

# Specific Heat of Liquid Helium in Zero Gravity very near the Lambda Point

J. A. Lipa,\* J. A. Nissen, and D. A. Stricker  
*Physics Department, Stanford University, Stanford, CA*

D. R. Swanson  
*Callida Genomics, Sunnyvale, CA*

T. C. P. Chui  
*Jet Propulsion Laboratory, Caltech, Pasadena, CA*  
(Dated: November 4, 2018)

We report the details and revised analysis of an experiment to measure the specific heat of helium with subnanokelvin temperature resolution near the lambda point. The measurements were made at the vapor pressure spanning the region from 22 mK below the superfluid transition to 4  $\mu$ K above. The experiment was performed in earth orbit to reduce the rounding of the transition caused by gravitationally induced pressure gradients on earth. Specific heat measurements were made deep in the asymptotic region to within 2 nK of the transition. No evidence of rounding was found to this resolution. The optimum value of the critical exponent describing the specific heat singularity was found to be  $\alpha = -0.0127 \pm 0.0003$ . This is bracketed by two recent estimates based on renormalization group techniques, but is slightly outside the range of the error of the most recent result. The ratio of the coefficients of the leading order singularity on the two sides of the transition is  $A^+/A^- = 1.053 \pm 0.002$ , which agrees well with a recent estimate. By combining the specific heat and superfluid density exponents a test of the Josephson scaling relation can be made. Excellent agreement is found based on high precision measurements of the superfluid density made elsewhere. These results represent the most precise tests of theoretical predictions for critical phenomena to date.

PACS numbers: 67.40.Kh, 65.20.+w

## I. INTRODUCTION

The renormalization group (RG) theory<sup>1</sup> has long been accepted as the basis of our understanding of critical phenomena due to its ability to deal with the problem of fluctuations on a wide range of length scales and to realistically predict many quantities of experimental interest. However, it is well known that precise quantitative predictions with correspondingly accurate experimental tests are few. Essentially all tests performed near gas-liquid critical points are unable to give detailed attention to the asymptotic region close to the phase transition, where the RG predictions are simplified and best established. Severe difficulties are encountered here due to transition broadening associated with gravity and relaxation phenomena, limiting the useful temperature range for tests of the theory. For example, near the critical point of a 1 mm high sample of xenon, density gradients cause substantial distortion of the singularity for reduced temperatures,  $|t|, \lesssim 10^{-4}$ , where  $t = 1 - T/T_c$  and  $T_c$  is the transition temperature.<sup>2</sup> This results in the observation of effective exponents which are perturbed from their asymptotic values by higher order terms, providing only weak support for the theory. To avoid this problem some experiments have been performed in space. For example, recent measurements<sup>3</sup> of the specific heat of SF<sub>6</sub> have extended about an order of magnitude closer to the transition than ground based experiments.<sup>4</sup> Relaxation phenomena now appear to inhibit further gains. In contrast,

at the lambda point of helium, the transition between He I and He II, a much wider range of  $|t|$  is accessible. On earth values of  $|t| \lesssim 10^{-7}$  can typically be reached<sup>5</sup> before finite size effects become the limiting factor. This has resulted in the lambda transition becoming the premier testing ground for the RG theory of second order transitions. In space, the lambda transition is expected to be sharp to  $|t| \approx 10^{-12}$  in ideal conditions.<sup>6</sup> Here the challenge is more to develop a measurement technique than to obtain a suitable sample.

Recently, improved predictions have been derived for a number of universal quantities of three dimensional critical systems.<sup>7,8,9</sup> These predictions now approach the accuracy of the corresponding experimental observations near the lambda point. This advance has uncovered a small but not entirely negligible discrepancy between the heat capacity exponent,  $\alpha$ , measured in a space experiment conducted in 1992<sup>10,11</sup> and the most recent predictions. Since this comparison currently represents one of the core tests of the RG theory, we have completed a more detailed analysis of the experiment with the aim of reducing systematic bias in the results as much as possible. We have also included additional measurements that were rejected earlier due to uncertainties in their calibration. The results of this analysis are presented here, along with a detailed report on the significant aspects of the experiment. We now find better agreement with the predictions than previously.

While the experiment was in principle very straightforward, the constraints of operation in space dictated a

TABLE I: Comparison of predicted and observed values of universal quantities near the lambda point.

Quantity	Predicted	Reference	Observed	Reference
$\alpha$	$-0.01126 \pm 0.0010$	7	$\sim -0.022 \pm 0.006$	15,16,17
$\alpha$	$-0.0146 \pm 0.0008$	8	$-0.0105 \pm 0.00038$	10,11
$\zeta$	$0.67015 \pm 0.00027$	8	$0.6705 \pm 0.0006$	18
$3\zeta + \alpha - 2$	0(exact)	20	$-0.0012 \pm 0.0027$	5,18
$\Delta$	$0.529 \pm 0.009$	25	$0.5 \pm 0.1$	22
$P$	$4.433 \pm 0.077$	9	$4.2 \pm 0.1$	23
$a_c^+/a_c^-$	$1.6 \pm 1.0$	24	$1.0 \pm 0.3$	23
$a_c^-/\alpha a_\rho$	$3.4 \pm 0.1$	24	$4.1 \pm 0.2$	23

number of compromises in the instrument design and the data collection procedures, which increased the complexity and the noise level. Because of the extreme cost of such experiments, it is unlikely that the measurements will be independently verified for quite some time. We have therefore attempted to provide sufficient detail in the sections below to allow a reasonably complete assessment of the strengths and weaknesses of the experiment.

The remainder of this section is devoted to a brief summary of the status of RG testing near the lambda point focusing on static exponents, and a discussion of the intrinsic limits expected in the present experiment. In Sec. II we describe the apparatus and in Sec. III we discuss the calibration and heat capacity measurements performed on the apparatus prior to the flight mission. The sequence of the flight measurements is described in Sec. IV and some post-flight measurements are discussed in Sec. V. In Sec. VI we present the analysis of the data and discuss its significance. We summarize in Sec. VII.

### A. Background

The lambda transition of helium is the primary example of the universality class with a two-dimensional order parameter in three spatial dimensions ( $n=2$ ,  $D=3$ ) and has a strong divergence of the correlation length, leading to easily measurable critical effects. In addition, the transition has a number of unique properties which can aid investigations. For example, the transition occurs at a line rather than at a point on the phase diagram, simplifying the experimental requirements compared to a liquid-vapor critical point. Also the compressibility is only weakly divergent, substantially reducing gravity effects. On the low temperature side of the transition the liquid is in the superfluid state, essentially free of temperature gradients. These features have enhanced our ability to perform a number of very high resolution investigations of the transition region.

Of primary interest for static phenomena near the lambda point are the behavior of the specific heat,  $C_p$ , and the superfluid density,  $\rho_s$ . In a quantitative analysis of the temperature dependence of these parameters it is necessary to deal with non-asymptotic representations

because data are obtained a finite distance from  $T_\lambda$ . In this region the RG theory predicts that<sup>12</sup>

$$C_p = \frac{A^\pm}{\alpha} |t|^{-\alpha} (1 + a_c^\pm |t|^\Delta + b_c^\pm |t|^{2\Delta} + \dots) + B^\pm \quad (1)$$

where the + and - signs refer to  $T > T_\lambda$  and  $T < T_\lambda$  respectively, and

$$\rho_s = \rho_o t^\zeta (1 + a_\rho t^\Delta + b_\rho t^{2\Delta} + \dots) \quad T < T_\lambda \quad (2)$$

Within the RG scheme, the quantities  $A^\pm$ ,  $B^\pm$ , and  $\rho_o$  as well as the correction amplitudes  $a_c^\pm$ ,  $b_c^\pm$ ,  $a_\rho$ ,  $b_\rho$  depend on pressure-dependent parameters of the statistical distribution of the order parameter, whereas the critical exponents  $\alpha$ ,  $\zeta$  and the confluent singularity exponent  $\Delta$  are independent of these parameters, i.e. universal. Certain ratios of the non-universal amplitudes are also predicted<sup>13</sup> to be universal, for example,  $A^+/A^-$ ,  $a_c^+/a_c^-$ ,  $a_c^-/a_\rho$ . It is also useful to define the quantity  $P \equiv (1 - A^+/A^-)/\alpha$  which is relatively stable when  $\alpha$  is small.<sup>14</sup> Using advanced analytical and numerical techniques it has been possible to derive estimates for many of the universal quantities, a number of which are summarized in Table I. Recently the bounds on the theoretical value of  $\alpha$  have been reduced substantially, allowing a higher quality test of the theory. Two recent predictions for this quantity are listed in the table.

In the case of  $\alpha$  the experimental situation is somewhat complex because of the differing conditions of various measurements. A number of experiments are in approximate agreement, but indicate a possible difference between the value of  $\alpha$  at the vapor pressure and that along the lambda lines as a function of pressure and <sup>3</sup>He concentration. Mueller et al.<sup>15</sup> obtained  $\alpha = -0.026 \pm 0.004$  from measurements of the isobaric expansion coefficient as a function of temperature and pressure. Gasparini and Moldover<sup>16</sup> performed measurements of the specific heat along the <sup>3</sup>He - <sup>4</sup>He lambda line at constant <sup>3</sup>He concentration. These data were fitted to Eq.(1) by Gasparini and Gaeta<sup>17</sup> assuming  $b_c^\pm = 0$ . Excluding the measurements for pure <sup>4</sup>He, they obtained  $\alpha = -0.025$ , in very good agreement with the expansion coefficient result. On the other hand, their pure <sup>4</sup>He results gave  $\alpha = -0.016$ . Some of the early ground measurements

from this program<sup>5</sup> gave  $\alpha = -0.0127 \pm 0.0026$  at the vapor pressure, and the previous analysis of the present experiment<sup>10,11</sup> gave  $\alpha = -0.0105 \pm 0.00038$ . While the differences are not large in absolute terms, the exponent results along the lambda lines do not appear to be entirely compatible with the vapor pressure measurements. In Table I we have indicated an approximate range of  $\alpha$  obtained from other groups and the previous result from the present experiment.

Recent values of  $\zeta$  obtained from second sound data at the vapor pressure are  $0.6705 \pm 0.0006$  by Goldner et al.<sup>18</sup> and  $0.67016 \pm 0.00008$  by Adriaans.<sup>19</sup> In the latter case the error quoted included only the statistical uncertainty from the velocity measurements. The results for  $\zeta$  and  $\alpha$  can be combined to test the exact scaling prediction<sup>20</sup>  $3\zeta + \alpha - 2 = 0$ . Combining the results of refs. 5 and 18 (for example) we obtain  $3\zeta + \alpha - 2 = -0.0012 \pm 0.0027$  at the vapor pressure. As yet, no high accuracy measurements of  $\zeta$  along the lambda lines have been reported. However, higher order departures from a truncated version of Eq.(2) have been shown<sup>21</sup> to be in good agreement with RG predictions.

## B. Factors Limiting the Exponent Determination

To obtain the best information on the divergence of the specific heat at a cooperative transition it is generally considered desirable to collect the most accurate data over the widest possible range. Both the inner and outer limits of this range are set by practical issues which either increase the noise of the results or lead to bias in the derived exponent. In the present experiment we have the potential for obtaining a statistical uncertainty  $\sigma_\alpha \sim 0.0002$  so we need to consider bias effects that could lead to systematic errors  $\Delta\alpha \sim 10^{-4}$ . We explore these and related issues in this subsection.

From an inspection of Eq.(1) it can be seen that the value obtained for  $\alpha$  is likely to be more reliable the smaller the value of  $t$  at which the curve fitting is done. This is because the higher order terms in the expression tend to zero in the limit of small  $t$ . However, technical difficulties increase in this region both due to measurement techniques and sample imperfections. It is easy to show that on earth the lambda transition will be severely rounded over a temperature interval of about  $1.3 \mu\text{K}$  per centimeter of hydrostatic head in a sample, due to the slope of the lambda line,  $(\partial P/\partial T)_\lambda$ . For a sample of constant cross-section and height  $h$ , the effect on the specific heat can be visualized as a convolution of a gravity-induced temperature ‘window’  $\Delta T_\lambda = \rho gh(\partial T/\partial P)_\lambda$  with the gravity-free function in Eq.(1), where  $\rho$  is the density of the fluid and  $g$  is the acceleration due to gravity. This approximation is valid because over the relatively small hydrostatic pressure heads encountered in typical calorimeters the pressure dependence of the specific heat can be neglected. The situation can also be understood by examining the P-T phase diagram of helium

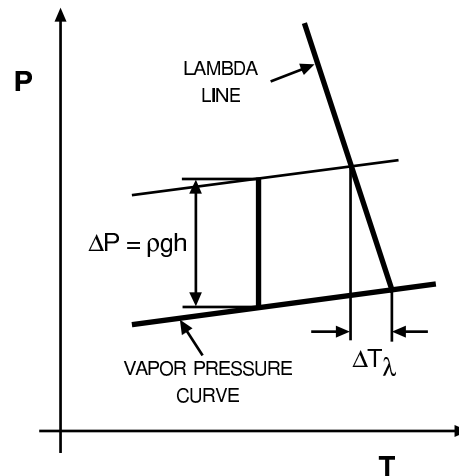


FIG. 1: Phase diagram for liquid helium near the intersection of the vapor pressure curve and the lambda line.

sketched in Fig. 1. The heavy tilted lines represent the vapor pressure curve and the lambda line. Also shown is a vertical bar representing the states of the fluid in an isothermal sample cell with a small vapor space and a moderate vertical height. It can be seen that some of the states are closer to the lambda line than others, even at constant temperature. As the sample is warmed through the transition it enters a two-phase region which persists over a temperature range given by  $\Delta T_\lambda$ . This hydrostatic pressure effect has been observed in numerous experiments.<sup>5,27</sup>

Clearly, smaller sample heights lead to less rounding, but soon a limit is reached where the height is so small that finite size effects begin to affect the results.<sup>11</sup> Normally this would occur at the angstrom level, but near the lambda point the correlation length,  $\xi$ , characterizing these effects diverges as  $\xi \approx \xi_0 t^{-2/3}$ , magnifying the effect enormously. This behavior is intrinsic to all cooperative transitions, being associated with the physics of the transition process in an essential way.

Using paramagnetic salt thermometry techniques a temperature resolution of  $< 3 \times 10^{-10} \text{ K}/\sqrt{\text{Hz}}$  is now routinely available near the lambda point, and in many cases signal averaging can improve this resolution substantially. To limit the hydrostatic rounding of the specific heat at the lambda point to a 1 nK range, for example, the height of a helium sample would have to be reduced to about  $10^{-3} \text{ cm}$ . But the divergence of  $\xi$  at the transition implies that such a thin sample would no longer exhibit bulk behavior.

By performing experiments in earth orbit the hydrostatic effect can be reduced substantially. This allows the use of larger samples to reduce the finite size effect and thereby obtain useful data at higher resolution. Unfortunately the acceleration environment on the shuttle is highly variable so it is not possible to apply corrections for the hydrostatic effect. A rough estimate of the magnitude of the effect can be obtained by considering

the effect of acceleration impulses of different duration. It is evident that impulses short compared to the measurement time will have no effect on the result except for higher order dissipation effects. On the other hand, impulses lasting as long as the measurement time will lead to a full hydrostatic effect. Thus we are led to consider the low frequency portion of the acceleration spectrum as a possible source of distortion of the heat capacity results. From the spectral measurements made during the mission we found the acceleration amplitude to be  $< 3 \times 10^{-5}$  g in the region below 1 Hz. Using this as an upper limit and a sample size of 3.5 cm we obtain a transition broadening  $\Delta T_\lambda < 1.3 \times 10^{-10}$  K. To determine the effect on  $\alpha$  we modeled the transition broadening as a gravity correction and obtained a perturbation  $\Delta\alpha < 5 \times 10^{-5}$ . Both these effects are well below the level of detectability in the present experiment.

The first order departure from the bulk specific heat in a finite system can be characterized as a surface specific heat term which has been measured for one and two-dimensional geometries. Since the magnitude of this effect is proportional to the surface area of a sample, the observed specific heat can be written approximately as  $C_{exp} = C_p + AC_{Surf}$ , where A is the surface area and  $C_{Surf}$  is the surface specific heat per unit area. The effect of the surface term on the value obtained for  $\alpha$  can easily be determined by modeling. For the calorimeter used here and fitting over a range  $10^{-9} < t < 10^{-2}$  we obtained a perturbation  $\Delta\alpha = 3.4 \times 10^{-5}$ , using the finite size measurements of ref. 11 to estimate  $C_{Surf}$ . Since this result was sensitive to the precision of the data close to the transition relative to that far away, we used the actual experimental uncertainties as described in section VI below to make the estimate. At the time the experiment was designed, the behavior of the surface specific heat was not known with any certainty, leading us to reduce the surface area relative to the sample volume as much as possible.

As one includes data further from the transition the curve fitting procedure becomes more difficult since more terms must be carried in the function to obtain an accurate representation of the specific heat. Neglect of these terms can lead to systematic bias in the remaining parameters that are evaluated. First we consider the effect of neglecting a fourth order term in Eq.(1),  $c_c^\pm |t|^{3\Delta}$ . Assuming for estimating purposes that  $c_c^\pm = 1$  and fitting our data set with and without the term, we find the bias from its neglect is  $\Delta\alpha \sim 8 \times 10^{-5}$ . While this can be ignored for now, it shows the importance of an appropriate functional form, especially in high precision experiments. Alternatively one can restrict the range of the fit to reduce the bias from the neglected terms, a trade-off that sets the practical outer limit of the curve fitting region.

The experimental situation is actually slightly more complex than indicated by Eq.(1) due to the possibility of regular background terms that have so far been ignored. A more correct representation of the measured specific heat is  $C_{exp} = C_p + C_{reg}$  where

$$C_{reg} = c_0 + c_1 t + c_2 t^2 + \dots \quad (3)$$

in which the  $c_i$  are constants. Clearly  $c_0$  can be absorbed into B in Eq.(1) but the effects of the other terms need to be considered. From the wide range behavior of the specific heat<sup>26</sup> where fluctuation effects are small we estimate  $c_1 \approx 2$  J/mole K. Thus for  $t = 10^{-2}$  this term contributes  $\sim 0.07\%$  to the specific heat, a small but detectable amount. It is fortunate that the exponent of the third order term in Eq.(1),  $2\Delta - \alpha \sim 1.07$ , is close to that of the second term in Eq.(3). Since the coefficients of the terms are fitted parameters, this allows us to consider the effect on  $\alpha$  of combining the two terms into one. To study this we made a set of simulated data in which the term  $c_1$  was included in the generating function, but then ignored in the fitting procedure. Again using the actual experimental uncertainties we found a bias  $\Delta\alpha \sim 5 \times 10^{-6}$  which is negligible here. The value of  $c_2$  is harder to determine, but it would appear to be similar to  $c_1$ . Even at  $t = 10^{-2}$  such a term contributes  $\ll 0.01\%$  to the specific heat and can be neglected. Thus for the present experiment a sufficiently good fitting function can be obtained by absorbing  $C_{reg}$  into the original expression in Eq.(1). The small price paid for doing this is that the experimentally determined third order coefficients no longer represent quantities of theoretical interest, and other coefficients may be slightly perturbed. In the analysis described below we consider various fitting functions and ranges and evaluate their impact on the results.

A number of other factors can lead to bias in the exponent. For our experiment the most important appear to be the calibrations of the temperature scale and the calorimeter heater circuit. These issues are discussed in the relevant sections below. Other less significant issues are the details of the thermodynamic path followed by the sample, the slight pressure dependence of the parameters in Eq.(1), and gravity gradient effects.

## II. APPARATUS

The apparatus developed for the experiment has been described elsewhere in some detail.<sup>28</sup> In essence it consisted of a spherical copper calorimeter attached to a pair of high resolution thermometers and enclosed in a thermal control system. The apparatus was located in a helium cryostat rigidly mounted in the shuttle bay. The central experimental issues for performing a high resolution specific heat experiment are temperature resolution and thermal control. Conventional low temperature germanium resistance thermometers (GRTs) are capable of resolving to  $\Delta t \sim 3 \times 10^{-7}$  with a power dissipation on the order of  $10^{-7}$  W. Higher resolution would require increasing the power input, which rapidly leads to unacceptable thermal offsets due to self-heating. Near the lambda point, the measurement power can also cause

variable temperature offsets due to the strong temperature dependence of the thermal conductivity of the sample. Since the goal of the experiment was to achieve a resolution of  $\Delta t \sim 5 \times 10^{-10}$  for the specific heat measurements, it was essential to develop a new type of high resolution thermometer (HRT). The device we constructed was based on paramagnetic salt thermometry commonly used at very low temperatures and is described below.

The heat capacity measurements were made by measuring the temperature change of the sample when a heat pulse is applied. Typically, the energy applied to the calorimeter was chosen so that the temperature step was significantly smaller than  $T - T_\lambda$ . To make heat capacity measurements to  $\sim 1\%$  accuracy near the transition, it is necessary to control the energy input to the sample to  $\sim 10^{-11}$  C Joules, where C is the heat capacity of the sample. In the present case, for a heater operating for a few seconds, this corresponds to applied power uncertainties of  $\sim 10^{-10}$  W. In addition, during the drift period used to measure the corresponding temperature rise, the uncontrolled fluctuations of the background power input need to be less than  $\sim 10^{-11}$  W on time scales of  $\sim 100$  sec. This shows that very careful thermal control of the sample environment is necessary. To achieve this, we built a four-stage thermal control system which used HRTs on the inner stage as fine control sensors. This control system was the major portion of the low temperature apparatus that comprised the flight instrument.

A third item of great importance was a helium cryostat capable of operating in earth orbit. We made use of a low temperature facility developed by NASA which can operate near 1.7 K in zero gravity.<sup>29</sup> The experiment was flown in late October 1992 on STS-52. The instrument and electronics were built by Ball Aerospace based on prototypes developed for earlier ground experiments.<sup>5</sup> The space-flight hardware was constructed to meet rigorous design constraints including use of high reliability parts, structural analyses to verify its ability to survive launch level vibrations, and specialized construction techniques for operation in the thermal and vacuum conditions of space. Particular attention was paid to shielding the instrument from electromagnetic interference (EMI). Spurious EMI had the potential of heating the calorimeter in an uncontrolled fashion and generating pick-up in the HRTs. Since it was not possible to perform realistic EMI testing prior to the flight a conservative design approach was taken where possible.

Careful attention was also given to the design and fabrication of low temperature seals to minimize the possibility of vacuum leaks. Sufficient low temperature sensors and heaters were provided that all critical instrument operations had backup capability. This approach was reflected as far as practical in the electronics with the exceptions of the computer, the communications port and the power supply. Ball Aerospace also supplied a preliminary version of the computer code used for controlling the experiment and transmitting real time data to the ground during the mission. This software was designed

to provide near-automatic operation in case of communication problems during the mission and to accept a wide range of commands to alter the parameters of the measurements.

### A. Thermal Control System

The basic design of the thermal control system was similar to that used for earlier ground-based heat capacity measurements.<sup>5</sup> A number of structural changes were made to improve its utility and its ability to survive launch. A schematic view of the system is shown in Fig. 3 of ref. 28. It consisted of a vacuum can 20 cm in diameter and 60 cm long surrounding four thermal control stages in series with the calorimeter (stage 5). Four HRTs were housed in the lower part of the assembly and surrounded by a thermal shield attached to the fourth stage of the thermal isolation system. Two of the HRTs were attached to the calorimeter and the others to the thermal shield. An end-corrected aluminum wire solenoid was wound on the outside of the lower portion of the vacuum can to allow the application of a uniform magnetic field to the niobium flux tubes of the HRTs.

The primary structural element of the thermal isolation system was a tripod with legs of stainless steel tubing attached to the lid of the vacuum can. Three triangles of high thermal conductivity copper intersected the legs of the tripod at intervals of about 3 cm. These triangles formed the first three stages of the isolation system and also served to stiffen the tripod. They were attached to the legs by brazing. The ratio of the thickness of the copper triangles to the wall thickness of the legs was chosen to provide good thermal grounding for heat flowing down the legs. A ratio of 10 was estimated to attenuate thermal leakage by a factor of about  $10^3$  at each joint. The ratio of the thermal resistance along a side of a triangle between two legs to that of a leg section between triangles exceeded  $10^3$ , heavily attenuating any thermal gradients that might exist in the tripod attachment assembly.

During the design of the system it was found that the HRTs attached to the calorimeter might be subjected to unacceptably high whiplash loads during launch. To alleviate this problem the structure between the vacuum can lid and the tripod base was softened by the addition of a flexible plate. This had the side effect of making the instrument somewhat acceleration sensitive at the resonant frequencies of the plate plus its load, primarily near 55 Hz. Vibration tests described elsewhere<sup>30</sup> were undertaken to characterize the heating due to variable accelerations and determine the effect of the resonances in the structure during the mission. The flexible plate was attached to the vacuum can lid by six stainless steel rods. Due to the configuration of the vacuum can and the cryostat, this lid was not in direct contact with the helium bath, reducing the cooling power available to the thermal control system. To rectify this problem we added flexible copper foil thermal links between the tripod and

a copper ring in the center of the cylindrical wall of the vacuum can which was wetted by the helium.

The innermost thermal control stage had a more complex structure, consisting of a ring, shield and HRT support assembly formed from annealed high thermal conductivity copper. The shield completely surrounded the calorimeter and the set of HRTs, acting as a baffle for stray thermal radiation and a shunt for residual gas conduction. The calorimeter was located near the apex of a second stainless steel tripod which was not in direct contact with the legs of the first.

The temperatures of stages 1-3 were actively controlled with heaters and GRTs configured in proportional-integral (PI) servo feedback loops. The tripods and isolation stages form a thermal network. With the temperature servos operating, each GRT acts as a node or ground point in a low pass filter which attenuates thermal variations from external sources such as the main helium bath. The price paid for this active filtering is heat dissipation in the stages. Thus as one moves inwards through the stages the uniformity of the thermal environment transitions from being dominated by external effects to being limited by internal dissipation. By the time the third stage is reached, the thermal inhomogeneities in the structure are expected to be dominated by the power dissipated in the GRT and the heater. Since the heater power is typically 10-100 times that dissipated in a GRT this effect can be minimized by reducing the offset between the operating temperatures of stages 2 and 3. The temperatures of the stages are otherwise adjusted to provide sufficient dynamic range for the servo systems to control transients.

The stage 4 thermal controller had two operating modes: a coarse mode with a GRT as sensor and a fine mode with a HRT as sensor, both using a digital PI control loop to drive a heater. In the fine operating mode it was found that the long term stability of its temperature,  $T_4$ , was limited primarily by drift of the HRT set point to about  $5 \times 10^{-14}$  K/sec. Short term stability ( $< 1000$  sec) was  $\pm 3 \times 10^{-8}$  K, limited by the ability of the servo system to reject the temperature fluctuations of stage 3. We note that this level of control was much better in the apparatus built for laboratory use,<sup>5</sup> with the deterioration traced to the stiffening of the flight apparatus for launch survival. Nevertheless, the degree of thermal control of the calorimeter was adequate. The effect of the fluctuations of  $T_4$  on the measurements can be estimated roughly as follows. The thermal resistance between the calorimeter and stage 4 was found to be  $2.18 \times 10^4$  K/W. Thus near the lambda point, where the sample heat capacity exceeded 50 J/K, the time constant,  $\tau$ , for heat transfer between the calorimeter and stage 4 was  $> 10^6$  sec. The transient behavior of this part of the system can be modeled as a low-pass thermal filter with a single pole roll-off. The amplitude of the swings of the calorimeter temperature,  $T_5$ , is given by  $\Delta T_5 \approx \Delta T_4 / 2\pi\tau f_4$ , where  $f_4$  is the frequency of the fluctuations of  $T_4$ . With  $f_4 \sim 10^{-2}$  Hz we obtain  $\Delta T_5 \sim 5 \times 10^{-13}$  K. In ground testing it was

found that with fine adjustment of  $T_4$ ,  $T_5$  could be stabilized to a drift rate of  $< 10^{-12}$  K/sec for up to one hour. This was more than adequate to achieve the desired level of uncertainty in the heat input during a heat capacity measurement. To minimize thermal gradients in stage 4 the temperature difference  $T_4 - T_3$  was typically reduced to 1 mK, limited by the calibration uncertainties over the operating range of the experiment and the control requirements of the stage 4 servo. A typical temperature profile of the thermal control system consisted of stage 5 at a given operating temperature, stage 4 in thermal equilibrium with it, and stages 1, 2 and 3 controlled at 30, 10 and 1 mK cooler than stage 4.

Thermal gradients in the calorimeter assembly were reduced by deactivating the GRTs during high resolution measurements and using the heater only when step temperature changes were desired. With  $T_5$  constant the potential sources of residual temperature gradients are then the effects of stray electrical power pickup, internal dissipation in the mechanical structure, gas conduction, and charged particle heating in space. During ground operations the limiting factor on thermal control of the calorimeter appeared to be variations in stray power pickup in the circuits attached to it. To reduce this effect all leads to the calorimeter were thermally anchored at all stages using sapphire posts, which minimized the capacitance to ground. Also the leads were made of twisted pairs and were equipped with capacitance shunts to ground where they entered the helium cryostat, which formed a complete metallic enclosure around the instrument. For the wiring to other stages, similar techniques were used, except that the sapphire was replaced with copper. The calorimeter was also thermally connected to stage 4 by four capillary gas lines and two HRT pickup loops with niobium-titanium shields. Special clamps were built to thermally anchor these lines to the isolation stages by sandwiching the lines between indium foil for good thermal contact. The length of the clamped sections was at least twenty times the diameter of the largest line. All leads and lines were fabricated from low thermal conductivity materials. In the case of leads to heaters, superconducting niobium-titanium wire was used, both to allow accurate heat input measurements, and to avoid dissipation elsewhere in the thermal control system. With these precautions, the stray power variations seen in ground testing were generally below  $10^{-11}$  W over periods of hours.

## B. Calorimeter

The helium sample was contained in a 3.5 cm diameter spherical cavity cut from very high purity (6N) copper<sup>31</sup> by electrical discharge machining. This technique was used to preserve the highly annealed state of the copper and its associated high thermal conductivity at low temperatures. From the measured electrical resistance ratio of  $\sim 5700$  between 300 and 4.2 K we estimated<sup>32</sup> its ther-

mal conductivity at  $T_\lambda$  to be  $\sim 140$  W/cm K. The cavity was formed in two pieces that were electron-beam welded together. The inside surface was left somewhat rough to promote thermal coupling with the helium. A magnified view of this surface is shown in Fig. 2.

An approximately-to-scale cross-sectional view of the calorimeter is shown in Fig. 3. The base of a valve assembly was electron-beam welded to the top of the calorimeter. The valve was sealed by pressing a gold-coated copper flat against a circular copper knife-edge. The sealing pressure was set by adjusting the length of a stack of 16 Belleville washers and the valve was opened by a pneumatic actuator. A high degree of cleanliness was required in the knife-edge area to obtain a reliable superfluid-tight seal. A filling capillary passed through the thermal control system to a second valve on the outside of the cryostat. A charcoal adsorption pump was attached to the capillary through a filter to trap any helium leakage through the low temperature valve. The base of the calorimeter provided attachment points for a pair of HRTs. A beryllium-copper support flange was welded around the bottom perimeter of the calorimeter to provide attachment points for the support tripod and the HRT flux tube holders. The HRTs were provided with large area contacts directly to the calorimeter and the mechanical support points of the tripod were isolated from the HRTs to the extent allowed by structural rigidity considerations. Two  $30 \Omega$  manganin wire heaters were wound in sections on three sapphire posts which were attached to the circumference of the calorimeter  $120^\circ$  apart to apply distributed heating. The heater sections were linked together with superconducting wire. Two GRTs were also attached to the calorimeter.

Near the end of the mission, before the shuttle landed, the helium cryogen was depleted, causing the calorimeter to warm and become pressurized. A removable burst disk allowed the pressurized helium to vent into the vacuum can. Because the calorimeter was classified by NASA as a pressure vessel, it was required to be doubly fail-safe against bursting. This resulted in the addition of two fixed burst disks to the calorimeter. These burst disk assemblies were designed to minimize the included volume of helium and were fabricated from high conductivity copper to minimize their thermal relaxation time. A pair of small heaters penetrated the calorimeter wall. These were designed to cause vaporization of the superfluid when activated, guaranteeing a thermodynamic path along the vapor pressure curve, in the unlikely event that natural bubble nucleation in space was inhibited.

After fabrication the inside of the cavity was lightly etched with an acid ‘bright dip’ solution to remove loose material, and inspected through the removable burst disk hole using a fiber-optic light pipe to check for splatter from the welding. No problems were found. The cavity was then ultrasonically cleaned and flushed with low residue ethanol until the filtered waste no longer showed particle contamination. The valve assembly and the final burst disk were then installed in a class-10 clean room. A

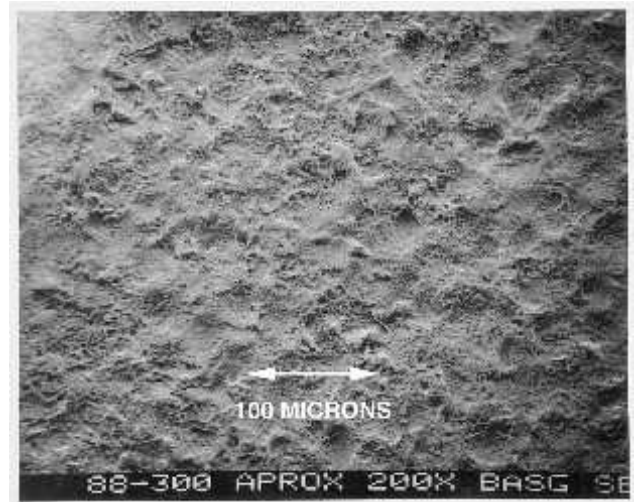


FIG. 2: Electron micrograph of the inside surface of the calorimeter showing the scale of roughening prior to assembly.

2-micron filter was placed in the fill line to guard against subsequent contamination.

### C. High Resolution Thermometers

The thermometers developed for the experiment made use of the strong temperature dependence of the magnetic susceptibility of copper ammonium bromide, CAB, and the high sensitivity of SQUID magnetometers to resolve very small temperature changes. The basic design and performance of the thermometers have been described extensively elsewhere,<sup>33</sup> but for completeness we include a brief description here, concentrating on those aspects relevant to the present experiment. The external portion of the HRTs consisted of a niobium tube 0.83 cm internal diameter and 18 cm long, with a constant magnetic field trapped along its axis. A 1.5 cm long cylinder of CAB was located near the center of the tube. The magnetic moments of the salt molecules were partially aligned by the magnetic field trapped in the flux tube. The magnetization of the salt changes with temperature, inducing a d.c. current in a superconducting pick-up loop surrounding the cylinder, which is measured by a SQUID magnetometer. A schematic view of the design is shown in Fig. 1 of ref. 28. The field was generated by the solenoid wound on the vacuum can and was trapped in the flux tubes early in the ground testing phase of the experiment. A reasonably comprehensive idea of the behavior of the thermometers as a function of temperature and magnetic field can be obtained by consideration of the Brillouin function applied to the behavior of CAB, which has a magnetic transition near 1.83 K.<sup>34</sup>

The pick-up coil and salt geometry were configured to maximize the sensitivity of the HRT. The optimization sets the coil diameter so that the cross-sectional areas of the tube inside and outside the coil are the same, when

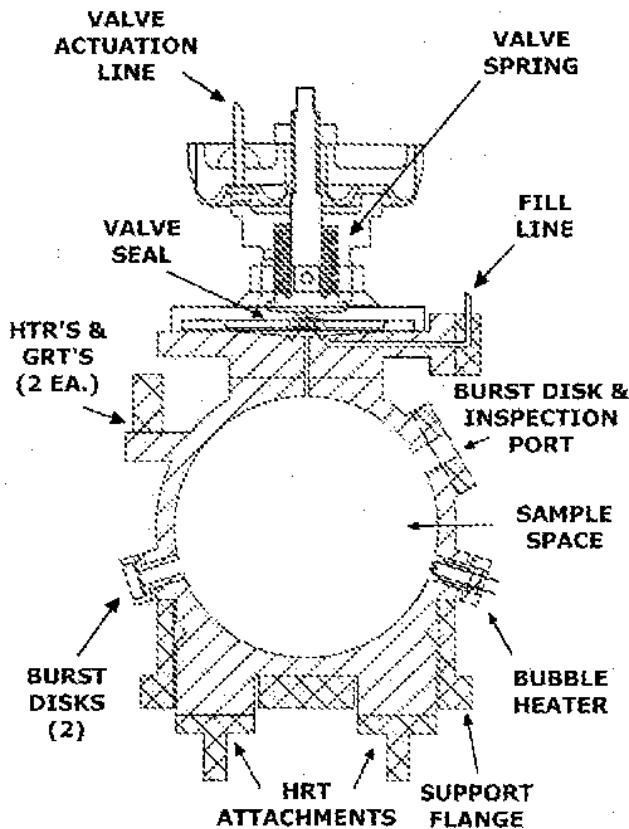


FIG. 3: Cross-sectional view of the calorimeter assembly, approximately to scale.

the salt fills the coil. The pick-up coil inductance was matched to that of the SQUID input coil for maximum energy transfer, and the number of turns around the salt was maximized for the highest sensitivity.<sup>35</sup> The coil and salt were placed in a sapphire holder which provided a high thermal conductivity link to the calorimeter without introducing Johnson noise currents. One end of the holder was metalised and soldered to a copper rod which thermally coupled the salt to the experiment. Copper wires embedded in the salt were also soldered to this rod to provide additional thermal contact. The rod was bolted to the base of the calorimeter using indium foil for thermal contact. The combined heat capacity of the salt pill and thermal impedance of the copper rod give a time constant of about 1 second for heat transfer between the salt and the calorimeter. The flux tube was held by a chrome-copper sleeve which was bolted to the support flange on the base of the calorimeter. The tube was a tight fit on the sapphire holder to reduce microphonics in the pickup coil.

The niobium-titanium leads from the pick-up coil were tightly twisted together, passed through a niobium-titanium tube for shielding, and attached to a SQUID located elsewhere in the thermal control system. The tube was filled with vacuum grease to promote thermal contact to the wires and to reduce microphonics. A heater

consisting of a short piece of 0.005 cm diameter manganese wire was wrapped tightly around one lead near the SQUID input terminals. Applying a 10 mA current to this heater warmed the pickup loop wire above its superconducting transition temperature in a fraction of a second, causing any persistent current flowing in it to decay rapidly to zero. This capability was included because it was found that some available SQUIDs were unable to operate with high currents in their input coils, limiting the dynamic range of the HRTs to a temperature band  $\sim 0.4$  K wide. By activating this heater with the calorimeter near the lambda point, a suitable operating range could be established. During early testing two other effects were detected. It was found that the HRT calibration was dependent on the temperature at which the current in the loop had been nulled. We therefore chose a small set of specific temperatures at which to null the current, as described in the calibration sections below. It was also found that a small apparent thermal coupling existed between the calorimeter and the outer stages of the thermal control system if a persistent current existed in the pickup loops. This effect was probably due to slight changes in the superconducting penetration depth of the pickup loop wire and shield with temperature at points where they were thermally attached to the stages. To minimize this effect the currents were again nulled within 1 mK of the transition.

To reduce the effect of the varying orientation of the HRTs with respect to the earth's magnetic field, three layers of shielding were used. The HRT flux tube itself had an extremely high theoretical shielding factor at the location of the pickup loop, but tests showed that this could be compromised by flux creep through the walls.<sup>36</sup> The practical shielding factor of this tube was expected to be  $\sim 5 \times 10^9$ . A second superconducting shield was added around the lower portion of the instrument vacuum can with a theoretical shielding factor of about 200. The third shield was a layer of moly-permalloy,<sup>37</sup> a high permeability material, placed around the outside of the cryostat to gain a further factor of 100. Tests of the complete assembly showed no detectable signal to a level of  $\pm 3 \times 10^{-4} \Phi_0$  for magnetic fields of  $10^{-4}$  T applied externally, where  $\Phi_0$  is the quantum of magnetic flux. In traversing an orbit, the experiment was subjected to a variation of about  $\pm 5 \times 10^{-5}$  T from the earth's magnetic field.

All the HRTs were grouped together below the calorimeter for convenient charging by the solenoid on the vacuum can. With the winding energized, the HRTs were warmed above 10 K and then cooled back to 4.2 K where the field was slowly reduced to zero. During this period the SQUID magnetometers remained near their operating temperature allowing the field trapping process to be monitored. It was found possible to detect the superconducting transition in the flux tubes and in the pickup coil wire. The field-to-current ratio of the solenoid was approximately  $1.1 \times 10^{-2}$  T/A and the field variation over the volume of the HRTs was measured to be  $< 1\%$ .



The trapped field level was selected as a compromise between the effects of digitizer nonlinearities and HRT drift performance. For a field of  $10^{-2}$  T trapped in the flux tubes, the sensitivities of the HRTs were typically in the range  $2 - 3 \times 10^6 \Phi_0/\text{K}$ . Their noise performance is discussed below.

#### D. SQUID Magnetometers

Four r.f. SQUID magnetometers were attached to an independent single-stage thermal platform supported from the lid of the vacuum can. This arrangement was necessary to minimize the effect of the temperature coefficient of the SQUIDs<sup>38</sup> on the HRT output, and to maintain the critical currents of the sensors within their operating range. The SQUID platform was stabilized to  $< 10^{-4}$  K using a servo similar to those on the outer stages of the thermal control system. The SQUIDs were housed in individual cylindrical niobium shields<sup>39</sup> closed at one end, with magnetic attenuation factors of  $\sim 5 \times 10^9$ . The open end of the tube was filled with a threaded niobium plug containing a small opening for the leads. Each assembly was placed inside a close-fitting Cryoperm<sup>40</sup> shield equipped with a degaussing coil. Before operation the SQUIDs and shields were warmed from their operating temperature of 4.5 K to above 10 K to reduce any internally trapped fields. They were then cooled slowly through the superconducting transition to minimize fields generated by thermoelectric currents.

The outputs of the SQUIDs were connected via triaxial cables to r.f. pre-amps and associated circuitry attached to the exterior of the cryostat. No modifications were made to the commercial 19 MHz r.f. SQUID sensors,<sup>41</sup> but the electronics were rebuilt to improve operation in space. They were strengthened to survive launch, repackaged to improve their thermal performance in vacuum and modified for computer-controlled tuning. The temperature of the pre-amps was controlled to  $\pm 0.1^\circ\text{C}$  to minimize d.c. offsets that would mimic temperature changes of the HRTs, and the A/D converters reading the outputs were controlled to about  $\pm 1^\circ\text{C}$ . In operation, the SQUID magnetometers give voltage outputs in terms of the magnetic flux change at the input, from which the corresponding changes in temperature of the salt pills can be inferred. The noise floor of the SQUIDs was on the order of  $10^{-4} \Phi_0/\sqrt{\text{Hz}}$ . The output bandwidths were limited to 0.16 Hz by double pole active filters.

#### E. Adsorption Pump

During early ground testing it was found that the launch vibration was capable of warming the HRTs on stage 4 to  $> 15$  K and the calorimeter to  $> 5$  K. Either of these temperature excursions could have ruined the experiment as there was no provision to re-magnetize the HRT flux tubes in flight and the pressure of the he-

lium in the calorimeter could have exceeded the set point of the removable burst disk. To reduce the temperature rise we placed approximately 0.3 mole of  $^3\text{He}$  exchange gas in the vacuum can prior to launch. This gas greatly increased the thermal coupling between the inner stages of the instrument and the vacuum can. Additional shake tests simulating the launch vibration indicated that the gas limited the temperature rise to  $< 0.1$  K. After launch, most of the gas was evacuated to space through the instrument vacuum pumping line. To obtain a high vacuum in the instrument during the heat capacity measurements an adsorption pump containing  $\sim 50$  cc of activated charcoal was located in the lid of the vacuum can. The charcoal container was thermally isolated from the lid allowing it to be heated to  $\sim 40$  K without significantly warming other components. The entrance to the pump was baffled with a gold coated copper disk which was thermally attached to the lid. This was needed to reduce the thermal coupling between the pump and stage 4 of the thermal control system.

To estimate the pressure in the system we monitored the power  $P_4$  dissipated in stage 4 of the thermal control system when the temperature difference  $T_4 - T_3$  was held at a specific value. During ground testing it was found that for pressures  $> 10^{-9}$  torr the additional power needed to compensate for the gas conduction was detectable. We roughly calibrated the rise in  $P_4$  against pressure using an external leak detector, allowing for thermomolecular effects. With no exchange gas in the system the pressure was typically  $< 10^{-9}$  torr, the limit of the measuring technique. When exchange gas was introduced, the pump-down time constant was on the order of a day, dependent on the vacuum can wall temperature. After about two days, the pressure in the vacuum can was generally low enough to perform high resolution measurements. However, the residual gas had small but detectable effects on the HRTs which were modeled and corrected for as described in the analysis section below.

#### F. Cryostat and Electronics

The cryostat system used to maintain low temperatures was inherited from a previous flight program.<sup>42</sup> No significant modifications were made to the cryogenic portions. However, the external supports were reconfigured to operate with a magnetic shield which was added to the exterior. The cryostat and its performance have been described elsewhere.<sup>43</sup> The liquid helium in the cryostat was cooled to  $\sim 1.7$  K during the flight by venting it to space through a sintered metal plug designed to contain the superfluid.

The instrument electronics consisted of nine 4-terminal a.c. resistance bridges, four r.f. SQUID controllers, four precision heater drivers with D/A converters and five analog servo circuits for temperature control. A number of digital switching circuits were also included. Five additional temperature controllers were used within the elec-

tronics to decrease the sensitivity of critical components to variations in the ambient temperature. The electronics were operated by a small PC-style computer with a 286 microprocessor and a basic software duty cycle of 1 Hz synchronized with a shuttle timing circuit. Once per cycle a 400 byte telemetry package was passed to a communications computer which also processed any commands sent from the ground. A third computer interfaced with the facility hardware to provide cryostat housekeeping functions. Most of the instrument tasks were broken into segments, limiting the amount of code executed in each cycle to avoid interference with the communication task.

The most critical circuits for heat capacity measurements were the heater current monitors and the A/D converters on the outputs of the SQUIDs. These converters had nominal 16 bit resolution, but were found to have occasional non-monotonic behavior of the output vs. input. Separate measurements indicated that the converters were likely to have  $< 2$  bits deviation from a straight line fit. Since the HRT noise level was typically 30 bits pp, substantial averaging over the bit errors occurred, reducing the corresponding temperature measurement errors significantly. For the heater current monitors the deviations from a linear fit were bounded by a  $\pm 0.01\%$  power measurement band over the full range of powers used in the experiment after corrections for the gains and offsets of the A/D converters.

The driver circuits for the heaters on the calorimeter had dedicated timers to allow precise control of the energy within a given heat pulse. The pulse time was accurate and stable to  $< 2$  parts in  $10^6$ . The rise and fall times were  $< 60 \mu\text{s}$  duration, giving a maximum correction of 0.0024% for the minimum 5 sec pulse length which was neglected. The heater driver circuit had 6 power ranges to accommodate a wide range of temperature step sizes while operating the A/D converters at a high bit setting. To allow automatic data collection a software routine was written to select the pulse length, power range and D/A setting optimum for a given temperature step. Manual operation was also possible.

Two plastic scintillators with photomultiplier tubes were attached to the exterior of the electronics. These were used as charged particle monitors (CPMs) for correlation with effects in the instrument. The voltage applied to each photomultiplier tube was programmable over a wide range to control the gain. The output of each CPM was threshold-detected at two levels, approximately 10% and 90% of saturation. The number of counts accumulated in each second for each channel of both detectors was included in the telemetry stream.

Two 3-axis accelerometers<sup>44</sup> with sensitivities of  $10^{-6}$  g were attached to the outside shell of the cryostat. The signals were sampled at 250 Hz and digitally filtered to a 100 Hz bandwidth. The vector amplitude of the acceleration was calculated and the peak value in each 1-second interval was output through a separate telemetry system to aid in characterizing the vibration environment. Occasional segments of raw data were also downlinked.

### III. PRE-FLIGHT OBSERVATIONS

Prior to its installation in the flight cryostat, the instrument was operated in the laboratory. In this period the volume of the calorimeter was determined by measuring the mass of gas extracted after a low temperature fill. In conjunction with data on the size of the small gas bubble left in the calorimeter near the lambda point, this information allowed us to determine the mass of the flight sample. The heat capacity of the empty calorimeter was measured, and the heater circuits were calibrated with board level and dummy load tests. Upper limits were set on variations of the stray power levels in the calorimeter heaters, and the GRT calibrations were checked in situ against a rhodium-iron thermometer<sup>45</sup> (RIT) calibrated by NIST.

After the instrument was installed in the flight cryostat, the flight sample was sealed in the calorimeter and the system was maintained at or below 4.2 K for an 18-month period while it underwent environmental testing and integration with the shuttle. During this period a number of checks were made to verify its correct operation. These included additional heater stray power measurements, a magnetic field susceptibility test, an electromagnetic susceptibility test, HRT calibrations, and lambda point observations on the GRT temperature scale. The instrument was shake-tested and the electronics were operated in a thermally controlled vacuum chamber. Heat capacity measurements were also made below the lambda point. The following subsections summarize the most critical measurements performed during the pre-flight period.

#### A. Thermometers

The GRTs on the calorimeter were calibrated by the manufacturer<sup>46</sup> and in the laboratory against the vapor pressure of  $^3\text{He}$  and the RIT using the ITS-90<sup>47</sup> temperature scale. For these measurements a specially built apparatus was used. The GRT resistance calibrations were performed using an a.c. bridge technique<sup>48</sup> with a seven-decade resistance standard<sup>49</sup> as the reference. The  $^3\text{He}$  calibration was performed using high purity gas and included corrections for thermomolecular and hydrostatic effects. In the range 1.8 to 2.4 K temperatures derived from the  $^3\text{He}$  calibrations deviated from those obtained from the GRT manufacturer's calibrations by about 0.5 mK on average, with a peak deviation of 0.7 mK. The RIT measurements were consistent with the  $^3\text{He}$  calibrations to within 0.3 mK over the interval 1.72 to 2.63 K. However it was found that the lambda transition temperature of a small sample of  $^4\text{He}$  was within 0.1 mK of that derived from the  $^3\text{He}$  calibration, leading us to prefer this scale for the experiment. The resistance values of the GRTs were converted to temperature using the

formula:<sup>50</sup>

$$\log T = a_0 + a_1 \log R + a_2 (\log R)^2 + a_3 (\log R)^3 \quad (4)$$

where the coefficients  $a_i$  were determined from least squares fits to the  $^3\text{He}$  calibration data. Between 2.0 and 2.4 K the deviations from the fits showed no significant trend exceeding their  $15 \mu\text{K}$  rms scatter. The bridges in the flight electronics were calibrated by the manufacturer (Ball Aerospace) and checked against our GRT bridge resistance standard mentioned above, which was separately checked by the JPL standards group. Corrections of up to  $0.4 \Omega$  from the nominal resistance values were stored in lookup tables in the flight computer. After the GRTs were installed in the flight instrument they were recalibrated against the RIT, which was then removed. It was found that the resistance vs. temperature scale factors of both GRTs appeared to have shifted by about 0.06% relative to that of the RIT, but by less than 0.01% relative to each other. This discrepancy appeared to be associated with a thermal anchoring problem with the RIT. Since measurements of the apparent temperature of the lambda transition also discriminated against the RIT, it was assumed that the GRT calibrations had not changed during installation. In either case, the absolute uncertainty in the values of  $(dR/dT)_\lambda$  appeared to be limited almost entirely by the 0.1% uncertainty in ITS-90.

Over the course of the experiment it was found that the apparent lambda transition temperature of one of the GRTs (#2) drifted slightly. While this drift was less than 0.2 mK over an 18-month period, it was substantially greater than the  $30 \mu\text{K}$  drift seen in GRT #1. Later measurements on a second flight experiment to measure the specific heat of confined  $^4\text{He}$ <sup>11</sup> confirmed the continued slight drift of GRT #2. We also found that the noise level of bridge #2 was a factor of 2.3 higher than that of #1. If we treat the drift as a scale factor change in the  $R(T)$  curve, we can estimate the change to be  $\sim 0.2 \text{ mK}/T_\lambda$ , or 0.01% which is negligible compared to the overall uncertainties of the experiment.

The HRTs attached to the calorimeter were calibrated against the GRTs over a 100 mK range just below the lambda point. This was done by repetitively bringing the apparatus into thermal equilibrium, recording the resistance and flux values, and then stepping the calorimeter temperature in increments of  $< 1 \text{ mK}$ . The HRT flux readings vs. GRT temperatures were fit over the full range using a Curie-Weiss model of the HRT salt behavior. The function used was

$$\phi - \phi_\infty = H_0(1 + a\phi)(T/T_c - 1)^{-\gamma} \quad (5)$$

where  $H_0$ ,  $\phi_\infty$  and  $a$  were constants determined in the fit, and the flux  $\phi$  was measured from the temperature at which the persistent current in the pickup loop was nulled. The term proportional to  $\phi$  on the right-hand side allows for the variation of the magnetic field with current in the pickup loop as the temperature is changed. We chose  $T_c = 1.8302 \text{ K}$  and  $\gamma = 1.2736$  based on the

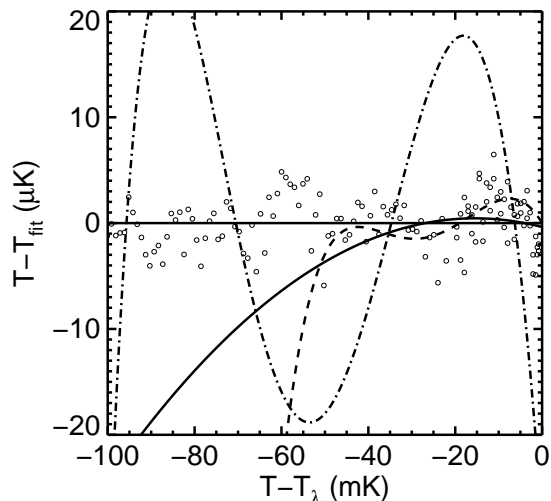


FIG. 4: Deviations of the GRT #1 data and various calibrations from the best fit of the HRT data to Eq.(5). The open circles are the GRT data, the dot-dash curve is a 3rd-order polynomial fit to the entire data set, the dashed curve is a 3rd-order polynomial fit in the range 0 to -50 mK, and the solid curve is a fit to Eq.(5) over the same restricted range.

data of Velu et al.<sup>34</sup> for CAB. Typical values obtained for the other parameters in Eq.(5) were:  $H_0 = 1.2158 \times 10^5 \Phi_0$ ,  $\phi_\infty = -1.5686 \times 10^6 \Phi_0$ , and  $a = -2.227 \times 10^{-7}/\Phi_0$ . In our earlier analysis<sup>10</sup> we used a third order polynomial in place of Eq.(5), fit over a 50 mK range. However we recently found that in the range  $3 \times 10^{-3} < t < 10^{-2}$  the heat capacity results were somewhat sensitive to the values of the second and third order coefficients. This effect led to a dependence of  $\alpha$  on the details of the HRT calibration procedure that exceeded our goal of no more than  $10^{-4}$  for systematic bias. The function in Eq.(5) gave results that were more stable in this outer region of  $t$ , and gave a better fit to the calibration data over a wider range of  $t$ . This can be inferred from Fig. 4 which contrasts the two calibration procedures. It shows the GRT data and various calibration curves as deviations from the best fit to Eq.(5) over 100 and 50 mK ranges. If we attempt to fit the data over the 100 mK range with a 3rd-order polynomial, we obtain the dot-dash curve: clearly a higher order polynomial is required for an adequate fit over this range. If we restrict the 3rd-order polynomial fit to 50 mK from  $T_\lambda$  as was done in the previous analysis of the flight data, we obtain the dashed curve. While this fit represents the data well in this restricted range, it rapidly deviates from the data set outside the fit range and more importantly it is overly sensitive to small local trends in the data set. In particular, the critical exponent, alpha, is sensitive to the curvature seen in the deviation plot of the 3rd-order polynomial in the range 0 to 20 mK below  $T_\lambda$ .

In the flight experiment, calibration data were only available over a 50 mK range so it is important to demonstrate that a Curie-Weiss model fitted over this restricted

range will still represent the data. The deviation of the Curie-Weiss model fitted over the 50 mK range from the fit over the full range is shown by the solid curve. It is clear that over the critical 20 mK range where heat capacity measurements were performed, the restricted Curie-Weiss model is superior to the 3rd-order polynomial fit. The curvature in the deviation plot over this range is substantially decreased, resulting in a reduction of systematic errors in the determination of  $\alpha$ . This new calibration procedure is chiefly responsible for the difference between the value of  $\alpha$  reported in ref. 11 and that reported here.

The statistical uncertainties of  $(d\phi/dT)_\lambda$  for the HRTs were  $< 0.004\%$  and no significant deviations were apparent between 2.12 and 2.177 K. It was found that the deviations from the fit tended to be large when a high bit was switched in the 16-bit reference resistors of the GRT bridges. We also found that the relays used for the switching often had a higher-than-specified resistance immediately after a contact had been closed. The calibration of the HRTs included the weighted data from both GRTs as well as 11 extra parameters for each GRT to model any additional contact resistance introduced by switching. The fit also included the constraint that the contact resistances are the same for the calibration of the two HRTs to ensure that there is only one GRT scale. These resistances were found to be  $< 0.33 \Omega$  in all cases, however, their inclusion reduced the scatter in the GRT readings by about a factor of two. The curve fitting process left a slight residual relative error in the temperature scales of the two HRTs. Since this resulted in slightly different heat capacity values depending on which HRT was used, we performed a second fit of the HRT data to a temperature scale defined by the average of the two.

To obtain reproducible calibration coefficients for the HRTs it was necessary to control the value of the persistent current flowing in the pickup loops. This current can perturb the field applied to the salt pill as shown in Eq.(5), changing its magnetization. We minimized this effect by setting the current to zero at fixed reference temperatures, using the heater attached to the HRT leads. The ground heat capacity data set was collected with the heaters activated while the HRTs were at 2.076 K.

The low frequency noise level of the HRTs was about  $2.5 \times 10^{-10} \text{ K}/\sqrt{\text{Hz}}$ , which is close to the value predicted by the fluctuation-dissipation theorem of Callen and Welton<sup>51</sup> applied to temperature fluctuations of a paramagnetic salt. The noise measurements have been described elsewhere.<sup>33,52</sup> Wide band random vibration tests were conducted to determine the various instrument sensitivities. It was found that the effect on the HRT noise was very nonlinear, being substantial above a r.m.s. vibration level of  $10^{-2} \text{ g}$  but relatively small below  $7 \times 10^{-3} \text{ g}$ . With the expected acceleration levels below  $2 \times 10^{-3} \text{ g}$  except for occasional transients, little effect on the thermometry was anticipated.

## B. Heater Power

There are two aspects of the calibration of the calorimeter heater power,  $P_5$ , that are relevant for the heat capacity results: measurement of absolute power parameters and an estimate of stray heater power. The heater resistance was measured at low currents to within 0.02% and the heater current monitor circuit was calibrated to 0.01% as mentioned earlier. The temperature coefficient of the heater resistance was also measured and applied in the analysis. The heater parameters could not be checked accurately in flight, but the heater current monitor circuit was tested in a thermal/vacuum chamber which simulated the space environment. Its calibration was found to be stable to  $\pm 0.01\%$  over the temperature range from  $-10^\circ$  to  $+30^\circ \text{ C}$ . During the experiment, the electronics box temperature was in the range  $18^\circ$  to  $23^\circ \text{ C}$ .

Residual or stray power dissipated in the heater can affect the heat capacity results if it varies between the heater 'on' and 'off' states. For example this could be caused by bias currents in the active elements of the circuit or by high frequency EMI that changes its level when the heater is switched. To reduce this possibility the heaters were terminated with resistive loads similar to those presented by the current supply circuits when switched to the 'off' state. Pulses were applied by first switching the heater power range and the associated D/A converter to the desired settings, then switching the heater from the resistive load to the circuit using CMOS switches controlled by a precision timer. By performing the switching from the 'off' to the 'on' state and leaving the D/A converter output at zero volts while monitoring the heating rate of the calorimeter, we were able to set a limit on the stray power change of  $< 10^{-11} \text{ W}$ .

A more comprehensive, though less precise test of the entire heat input circuit can be performed by comparing heat capacity values as a function of power. A special sequence of heat capacity measurements which consisted of a set of pulses covering the range of available power was performed at a temperature where the heat capacity is only weakly temperature dependent,  $\sim 20 \text{ mK}$  below the transition. Since the sample heats slightly as the pulse sequence progresses, a symmetrically arranged reverse sequence was also performed. By fitting the heat capacity results at the same power with a model function, the effect of the temperature dependence of the specific heat could be minimized. These measurements were made on a number of occasions and typical results are shown in Fig. 5. From the measurements we concluded that the apparent change in the stray heater power during pulses was  $-9.4 \times 10^{-11} \text{ W}$ . Since this was significantly higher than the value obtained in the zero input voltage switching test above, we concluded that most of the effect was due to a zero offset in the measurement circuit. It was also found that the apparent heat capacity decreased by  $\sim 0.17\%$  at the highest power used, possibly due to self-heating in the heater assembly. These effects were mod-

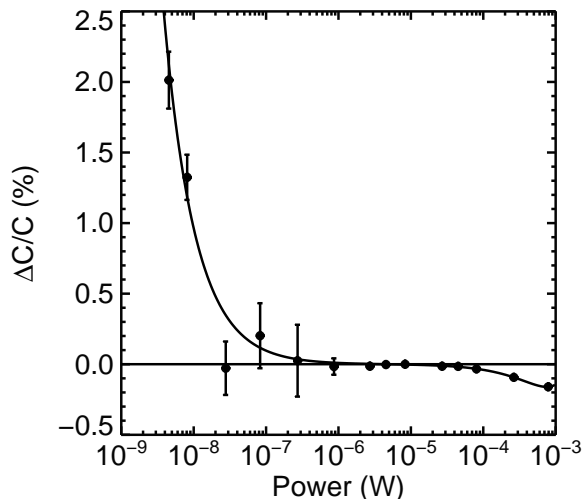


FIG. 5: Dependence of the apparent heat capacity on the power dissipated in the heater as measured during pre-flight testing. Curve shows model fit.

eled with a four-parameter function and corrections were applied to all pulse power estimates. For  $P_5 > 10^{-5}$  W the uncertainties in the fit were  $< 0.005\%$ .

Mechanical vibration was also expected to be a variable heat source during the flight experiment. From the vibration testing mentioned earlier we derived a calorimeter heating sensitivity of  $\sim 0.2$  W/g<sup>2</sup>/Hz using wide band random vibration input with power spectral densities in the range  $3 \times 10^{-6} - 2 \times 10^{-7}$  g<sup>2</sup>/Hz. With a swept sine wave input we determined that about 95% of the heating occurred in a narrow frequency band near 55 Hz. Since spectral densities of  $10^{-9} - 10^{-10}$  g<sup>2</sup>/Hz were expected in the mission, some low level heating from this source was anticipated. Unfortunately it was not possible to add vibration isolation to the apparatus due to cost.

### C. Sample Mass

The apparatus used to fill the calorimeter did not allow an accurate measurement of the quantity of helium sealed inside. Instead, we measured the sample mass by a two-step process which first involved measuring the calorimeter volume and the mass of a reference sample. The mass of the reference sample was measured during its extraction from the calorimeter. The volume was estimated by taking advantage of the very well known<sup>53</sup> temperature dependence of the density of helium along the vapor pressure curve near the lambda point. If the calorimeter is between 99.5 and 100% full at the lambda point, the gas space can be reduced to zero by cooling to a temperature  $2.18 > T_B > 1.8$  K. Above  $T_B$  the thermodynamic path is close to that of the saturated vapor pressure, while below  $T_B$  it is at constant volume. The passage through  $T_B$  can be detected by the small

but sharp change in the specific heat due to the change in the thermodynamic path. We were able to use  $T_B$  as a very sensitive indicator of the calorimeter fill fraction at the lambda point. The number of moles in the reference sample and the molar volume at  $T_B$  can easily be used to derive the calorimeter volume, resulting in a value of  $22.332 \pm 0.01$  cc. Combining this value with that of  $T_B$  for any other sample is then sufficient to determine its mass. An error of 1 mK in  $T_B$  corresponds to a mole number change of  $< 0.0015\%$  which is negligible compared with the uncertainty in the calorimeter volume.

The variation of the calorimeter volume from fill to fill was extremely small due to the design of the fill line valve. Closure was accomplished with a metal-to-metal seal with constant applied force. On the calorimeter side of the valve the variable volume was  $< 2 \times 10^{-3}$  cc during the seal indentation process. It is unlikely that the variation in volume after achieving a seal exceeded  $10^{-3}$  cc, which is negligible compared to the total volume. After the calorimeter was filled with the flight sample,  $T_B$  was again determined. The corresponding helium mole number was  $0.81314 \pm 0.0004$  and the gas space at the lambda point was estimated to be  $0.0558 \pm 0.0007$  cc.

### D. Empty Calorimeter Heat Capacity

The heat capacity of the empty calorimeter was determined by heat pulse measurements and indirectly from its relaxation time plus the thermal resistance to stage 4. Both methods gave consistent results. The heat capacity of the empty calorimeter at the lambda point was found to be  $0.0441 \pm 0.0005$  J/K, which agrees with a rough estimate based on the knowledge of its components. The temperature dependence of the heat capacity was measured to be  $0.019 \pm 0.003$  J/K<sup>2</sup>, which is negligible over the 20 mK range of interest. Nevertheless, a correction for this effect was applied.

### E. Ground Specific Heat Measurements

The basic method of measuring heat capacity was to establish a suitably low drift rate for the calorimeter temperature, apply a heat pulse of 5 - 35 s duration and then wait for the drift rate to return to a low value. The heat capacity was then computed in the usual way from the rise in  $T_5$  and the energy dissipated. Since the time constant for the relaxation of  $T_5$  to  $T_4$  was  $\sim 10^6$  s, simple linear extrapolation to the center of the pulse was generally sufficient to obtain the temperature rise. A least squares straight line fit was made to 50 - 120 s of drift data on each side of the pulse and the temperature change and value at the center of the pulse were estimated. The fitted data did not include the first 6 to 30 seconds of data after the heater was turned off. This was done to allow for the settling of small transients due to the warming of the calorimeter support structure and the Kapitza

boundary resistance, which slightly distorted the measurements. Near the lambda point it was necessary to reduce the size of the temperature steps to maintain accurate measurements of the local heat capacity and to achieve the desired resolution of the singularity. This resulted in a deteriorating signal/noise ratio as the transition was approached.

A software routine was used to generate a sequence of measurements that adjusted the size of the steps in a predetermined fashion and established the flux reading of the HRTs that corresponded to  $T_\lambda$ . The routine started by adjusting  $T_4$  to reduce  $\dot{T}_5$  below  $10^{-10}$  K/s. A heat capacity measurement with a moderate energy input was then performed and the specific heat was calculated. The remaining temperature increment to the lambda point was then estimated by comparing the measured specific heat with a functional form based on previous experiments. To avoid ambiguity this routine was used only below the transition. For subsequent measurements in the sequence the routine used the estimate to determine the energy input to the heater to give a temperature step  $\Delta T$  equal to a specified fraction of the remaining interval to the transition. Prior to each pulse  $\dot{T}_5$  was measured and adjusted to  $< 10^{-12}$  K/s or  $2 \times 10^{-4} \Delta T$  K/s, whichever was greater. After each pulse the estimate was updated. The routine allowed rapid collection of data approximately equally spaced on a logarithmic temperature scale, a distribution desirable for the final curve fitting task. It also maximized the time available for repeat measurements at high resolution that were necessary to improve the signal/noise ratio.

When used far below  $T_\lambda$  the routine also generated a string of alternating low and high power pulses. The low power pulses were performed to provide results over a wide range of  $t$  at a fixed low power in case unexpected power-dependent effects were detected in the analysis. The typical step size for these pulses was  $1 \mu\text{K}$  and the heater power was  $8 \times 10^{-6}$  W. The high power pulses started with the maximum power available,  $8 \times 10^{-4}$  W, and were designed to warm the calorimeter about 10% of the remaining distance to the transition. For  $t \sim 0.01$ , a pulse duration of 35 s was used, decreasing as the transition was approached. When the desired temperature step fell below  $300 \mu\text{K}$ , the high power pulses were discontinued.

The pulse method gives the specific heat integrated over  $\Delta T$ , which differs from the value at the midpoint temperature due to the curvature of the specific heat function. A correction given by  $\Delta C = \Delta T^2 (\partial^2 C / \partial T^2) / 24$  can be made if the function is known. To evaluate the second derivative we used the specific heat function given in ref. 5. This correction was  $< 0.07\%$  of the specific heat for all pulses.

Given the total specific heat of the sample,  $C_T$ , some additional small corrections are needed before a fit with a theoretical expression is performed. The presence of a gas space introduces small corrections to the specific heat primarily via the expansion coefficient and the la-

tent heat.<sup>54,55</sup> The most important effect is due to the changing volume of the gas space with temperature and the correction is given by

$$C_S = C_T / n_l + \alpha_s L \rho_g / \rho_l \quad (6)$$

where  $C_S$ ,  $\alpha_s$ ,  $n_l$ ,  $\rho_l$  and  $L$  are the specific heat, expansion coefficient, mole number, density and latent heat of the liquid, and  $\rho_g$  the density of the gas. This correction term is independent of the size of the gas space, but depends on its rate of change with temperature. A much smaller term, dependent on the volume of the gas, was also carried in the analysis. Another correction term is from the conversion of the specific heat along the vapor pressure curve to the specific heat at constant pressure.<sup>20</sup> The primary correction term is given by

$$C_p = C_S + T v \alpha_p (\partial P / \partial T)_{svp} \quad (7)$$

where  $v$  is the molar volume of the liquid,  $\alpha_p$  is the isobaric expansion coefficient<sup>15</sup> and  $(\partial P / \partial T)_{svp}$  is the slope of the vapor pressure curve. Other corrections for conversion to a constant pressure path were found to be negligible. The corrections to the specific heat in Eqs. 6 and 7 are small,  $< 0.1\%$ , but not entirely negligible in the experiment. The change of  $\alpha$  due to these corrections was found to be  $< 10^{-5}$ .

With the heat pulse method the fractional uncertainty in  $C$  is just  $(\sigma_C / C)^2 = (\sigma_Q / \Delta Q)^2 + (\sigma_T / \Delta T)^2$  where the  $\sigma$ 's are the corresponding uncertainties in the energy input and temperature step measurements. As described above,  $P_5$  was modeled to  $\sigma_Q / \Delta Q \sim 0.005\%$  at the higher power ranges while the overall accuracy was  $\sigma_Q / \Delta Q \sim 0.01\%$ . This was typically less than the fractional uncertainty in the temperature step,  $\sigma_T / \Delta T$ , especially near the lambda point. To obtain good precision at high resolution it was therefore necessary to average as many measurements as possible. The absolute uncertainty of the results depends not only on the noise but also on the accuracy of the heater and thermometer calibrations. However, the uncertainty of the best fit exponent is not dependent on the overall scale factors that affect the specific heat: instead it is set by the noise level of the data, its range, any temperature dependence of the scale factors, and the fidelity of the curve fitting function. The statistical uncertainties we used for the results were based on the formula above which gave values as low as  $\sigma_C / C = 0.008\%$ . We note that this does not include the  $\sim 0.1\%$  systematic uncertainty from ITS-90, nor the  $0.05\%$  uncertainty in our determination of the sample mole number. We estimate the absolute uncertainty in our specific heat values to be about  $\pm 0.2\%$ .

The results obtained for the specific heat prior to the flight are shown in Fig. 6 on a semi-logarithmic scale. Close to the transition the curve is distorted by the effect of gravity on the sample. This leads to a rounding of the singularity over a range of about  $5 \mu\text{K}$ . A magnified view of this region is shown in Fig. 7 on a linear temperature scale. The solid lines indicate the expected

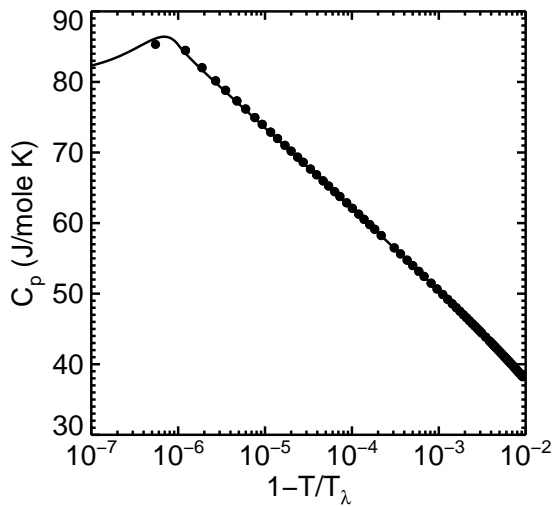


FIG. 6: Ground specific heat results below  $T_\lambda$  on a log-linear scale. Line: gravity rounded model.

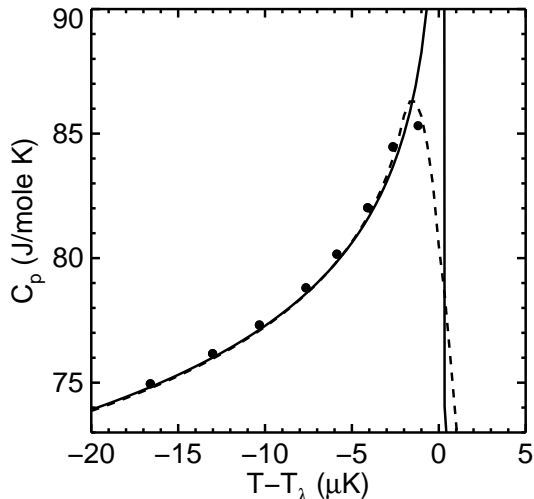


FIG. 7: Ground specific heat results on a linear scale close to the transition. Solid line: zero gravity function; broken line: gravity rounded model.

behavior in the absence of gravity based on our current fit to the flight data. The broken line shows the expected curve in the presence of gravity. The transition temperature was estimated by analyzing the thermal overshoot that occurs after a pulse which causes the helium to enter the two-phase region where normal and superfluid coexist within the calorimeter. We obtained an uncertainty of  $\pm 54$  nK in the temperature at which normal fluid was first stable within the calorimeter. In Fig. 8 we show the data as deviations from a zero-gravity reference function given below by Eq.(9), with parameters determined by a fit to the flight data. It can be seen that there is an offset of about 0.07% between the data and the function. We

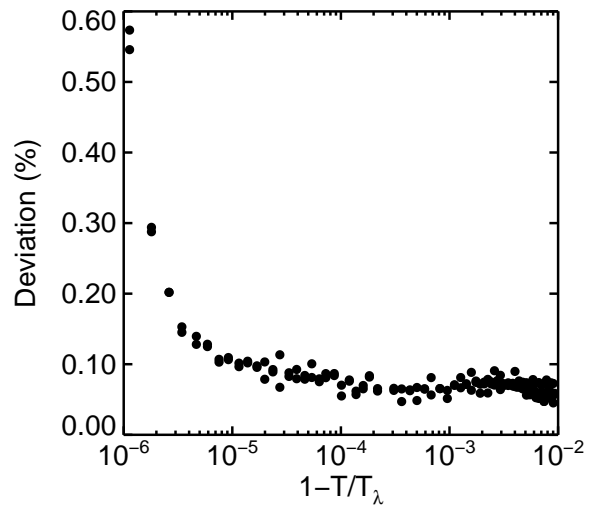


FIG. 8: Fractional deviations of ground specific heat results from the zero-gravity function.

believe this is due to slight changes in the calibration of the HRTs and heater circuit between ground and flight. Otherwise there is good agreement with the general behavior of the function up to the region where gravity effects become significant.

## IV. FLIGHT OBSERVATIONS

### A. Measurement Sequence

In this section we summarize the main events of the experiment, starting with the final refill of the cryostat on the launch pad at the Kennedy Space Flight Center. Because the duration of the experiment was limited to 10 days the flight measurements were performed in a sequence designed to obtain the results of most value as quickly as possible. A conflicting requirement was to re-calibrate the instrument to verify its performance and provide links to other specific heat measurements. As a compromise a limited calibration was performed early in the sequence as the calorimeter was warmed towards the transition for the first time. In this period the HRTs were re-calibrated against the GRTs and the power dependence of the heat capacity results was measured. The experiment was run automatically by its computer until the second day of high-resolution measurements. Manual control was then established to optimize the data collection by allowing for the effects of cosmic rays and heating from particles trapped in the magnetosphere over the South Atlantic ocean. The remainder of the flight period was devoted to heat capacity measurements near the transition.

Shortly before launch the instrument was cooled from 4.2 K to about 1.7 K, the cryostat was refilled with super-

fluid and  $^3\text{He}$  exchange gas was placed in the instrument vacuum space to provide a cooling path to the bath for heat dissipation in the instrument during launch. About two hours after launch the experiment was switched on and the calorimeter temperature was found to be close to 2.02 K. A motor-driven valve on the instrument evacuation line was opened and the charcoal adsorption pump in the vacuum can was warmed to  $\sim 40$  K to purge it of  $^3\text{He}$ . When the pressure in the vacuum can fell below an estimated 100 microns the valve was closed and the adsorption pump was cooled. The cryostat was also warmed to its maximum safe operating temperature in space, close to 2.1 K, to aid in releasing adsorbed  $^3\text{He}$  from the vacuum can walls. While the cryopump was reducing the pressure in the instrument, some preliminary tasks in the measurement sequence were performed. The first step involved warming the SQUIDs above their superconducting transition temperature ( $\sim 9$  K) and cooling them slowly to 4.5 K. This reduced any flux trapped in the SQUID junctions and in the shielding tubes, improving performance. The next event of significance was the spontaneous generation of a small helium bubble in the calorimeter which established a thermodynamic path at the vapor pressure for the heat capacity measurements. Shortly after the bubble was formed, the cryostat venting rate was increased, allowing it to cool to its minimum operating temperature of  $\sim 1.7$  K. This step allowed the calorimeter to be brought under thermal control and also produced significant cryopumping of the residual  $^3\text{He}$  gas on the vacuum can walls.

The next step was to prepare the instrument for high resolution measurements. To do this, the various stages of the thermal isolation system were brought to their normal operating temperatures which were kept as close as practical to that of the calorimeter. The heaters on all the HRT pickup loops were then activated to null the circulating persistent currents. Next, the HRT calibration procedure was performed between 2.126 and 2.156 K. The stage 4 servo was then set to the fine control mode and the drift rate of the calorimeter temperature was reduced to a value acceptable for heat capacity measurements. It was possible to reduce this drift rate to  $\sim 10^{-12}$  K/s with little difficulty by varying the stage 4 temperature, however, variations of heating from the charged particle flux made it difficult to maintain this level of stability for more than a few minutes. When the pressure in the vacuum can approached the  $10^{-9}$  torr range the calibration sequence was continued. At this point the power dependence of the heat capacity results was measured. This step also verified that the heater driver circuit was operating normally.

After the heater circuit test was completed, the primary heat capacity measurements were commenced. Since there was insufficient time in the mission to collect more than one wide range data set, the final 20 mK of the HRT calibrations was interwoven with the heat capacity measurements. The GRTs on the calorimeter were deactivated about 1 mK below  $T_\lambda$  to reduce tem-

perature gradients in the calorimeter. The heater on one of the calorimeter HRT pickup loops was again activated at 709  $\mu\text{K}$  below the transition, setting the current in the loop to zero once more. This was done to minimize a small magnetic coupling effect between the isolation stages described earlier. While the pickup coil leads were in the non-superconducting state, a small quantity of flux was not measured by the SQUID. This discontinuity was corrected for by noting the flux change on the second calorimeter HRT during the time the heater was on. At 13  $\mu\text{K}$  below the transition the current in the pickup loop of the second HRT was nulled. Again, the flux discontinuity was corrected by using the readout of the alternate HRT.

When the calorimeter was 92 nK below the transition, the high resolution measurement mode was activated. In this mode the pulse size estimator was disabled and a set of pulses of constant energy was applied to the calorimeter heater. This set was designed to warm the calorimeter through the transition, terminating about 10 nK on the high temperature side. Another routine was then used to cool the calorimeter by about 50 nK. After repeating this cycle ten times the automatic operating mode was terminated and the instrument was operated from the ground. Typical measurement sequences in this phase consisted of sets of 5 to 10 pulses of 1 to 10 nK size starting 10 to 30 nK below the transition. Each set was followed by a cooling ramp at a rate of  $\sim 100$  pK/sec to the starting temperature for the next set. The location of the lambda point on the HRT flux scale was found to within  $\pm 2$  nK by observation of the transient overshoot of the calorimeter shell after a pulse, due to the finite thermal conductivity of the helium above the transition. In later analysis more precise determinations were made by modeling the behavior of the cooling rate as the calorimeter passed through the transition. After the region near the transition was well covered, heat capacity measurements were extended a few  $\mu\text{K}$  on the high temperature side. In this region estimates of the thermal conductivity can be obtained from the relaxation data. These measurements were taken on a time available basis and were not expected to approach the accuracy of the results on the low temperature side. After about 10 days of operation the cryogen was exhausted and the experiment was terminated. The details of the significant portions of the measurement sequence are given below.

## B. Bubble Detection

An important aspect of the experiment was to ensure that the measurements of heat capacity were performed along a thermodynamic path that is as close as possible to constant pressure. This was done by allowing a small bubble of vapor to form in the calorimeter, taking advantage of the slightly higher density of liquid helium in the region very close to the lambda point. As the sample of helium is warmed from the starting temperature near 2



K towards the lambda point, the liquid shrinks slightly, generating a bubble. This event occurs spontaneously due to the metastability of the thermodynamic state, as opposed to the equilibrium collapse behavior observed at  $T_B$  on cooling.<sup>56</sup> Nucleation of the bubble can be triggered by an imperfection on the calorimeter wall or by the passage of a charged particle through the fluid. In ground testing the resulting sharp change of the heating rate of the helium was found to occur within 1900 seconds of entering the metastable region. In flight the event occurred about 1863 seconds after entering the region, but at 2.079 K vs. 2.076 K on the ground. In zero gravity the states occupied by the sample on the helium phase diagram are slightly different to those on earth. On average, this effect would cause the bubble to be formed at a temperature about 20  $\mu\text{K}$  warmer in space, all else being equal. From these observations we conclude that near 2 K the probability of nucleating a stable bubble in superfluid helium by a cosmic ray must be  $< 10^{-4}$  for pressures on the order of 2000 Pa below the vapor pressure. The temperature of the bubble event can be used to set limits on the amount of helium in the calorimeter. Since the bubble event occurred at a slightly warmer temperature in flight, this was an indication that no helium had been lost from the calorimeter and the pre-flight mole number was still valid.

### C. Flight Calibration of HRTs

As noted earlier, comparison of the resistance values at the lambda point of the two GRTs on the calorimeter over the whole experiment period indicated that GRT #1 was slightly more stable than #2. For GRT #1 no offsets greater than 30  $\mu\text{K}$  were detected over the 8 months prior to flight, essentially the limit of our measurement capability. It was also found that the noise on bridge #1 continued to be lower than that on #2. Due to the constraints of the mission the HRTs were calibrated over the range 2.126 to 2.176 K, half that of the ground calibration. A set of 76 data points spaced at  $< 1$  mK intervals was used to calculate the coefficients of the best fit function in Eq.(5). The measurements were analyzed in a similar way to the ground calibration data. A study of ground measurements showed that the smaller range could lead to some bias in the parameter values obtained from the curve fit. We also found that the value of the parameter  $a$  in Eq.(5) was extremely stable from calibration to calibration. We therefore decided to fix it at the ground value in the analysis of the flight data and only fit the other two parameters. This approach was shown to significantly reduce the bias. In Fig. 9 we plot the resulting differences between the GRT #1 temperatures and the HRT temperatures derived from Eq.(5), as a function of GRT temperature. The noise in the plot is almost entirely due to the GRT measurements. It can be seen that there is little systematic deviation from the function over the entire range of the data. The relative

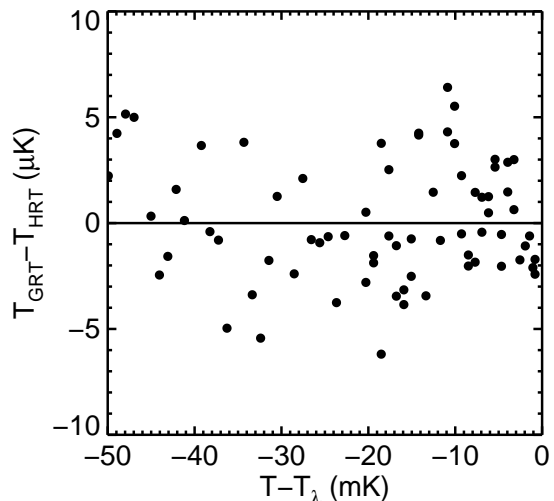


FIG. 9: Flight calibration data for GRT #1 on the calorimeter vs. the HRT scale.

deviations of the two HRTs over the range used in the heat capacity measurements were within  $\pm 35$  nK, and the maximum slope difference was  $< 5$  parts in  $10^6$ . Close to the transition the temperature offsets were reduced to  $< 5 \times 10^{-10}$  K when estimates of the lambda transition temperature became available. Comparison with the ground calibrations showed only very small changes,  $< 0.045\%$  in  $d\phi/dT$  at the lambda point. Also, the apparent value of  $T_{\lambda}$  on the GRT #1 temperature scale changed by  $< 3 \mu\text{K}$ , giving us confidence that there was little change of the absolute calibrations in flight.

Since it was not possible to obtain sufficient data to directly calibrate the HRTs with the persistent current nulls made within 1 mK of the transition, a cross-calibration technique was used. By activating only one heater at a time and spacing the nulling temperatures by  $\sim 700 \mu\text{K}$  it was possible to piece together the changes in the values of  $d\phi/dT$  to high accuracy. For the first section a third order polynomial was used and for the second, shorter region a second order polynomial was used. This is all that is needed for the close-in heat capacity data since curvature effects from the calibration in this region are small. We obtained an uncertainty in the values of  $d\phi/dT$  relative to those from the wide range calibration of  $< 0.0075\%$ , which is negligible compared with the noise of the heat capacity data.

### D. HRT Noise

The noise on the HRTs was significantly larger in flight than on the ground. The excess noise appeared to be related to the charged particle flux passing through the HRTs. Protons and alpha particles passed through the HRTs on the order of once per second. Due to the 1 second time constant of the thermal link between a HRT and

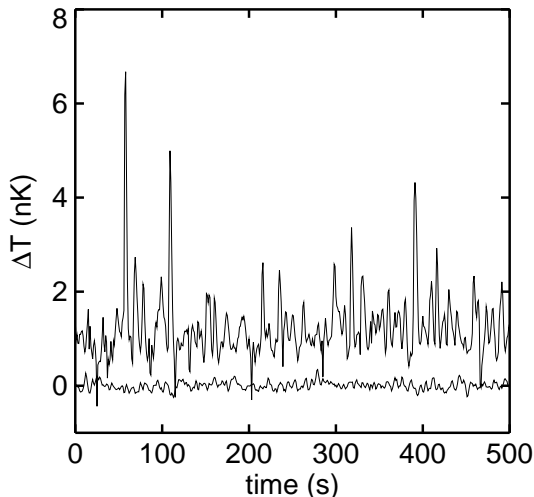


FIG. 10: HRT noise measurements. Upper curve: noise seen during the mission. Lower curve: similar data collected during ground testing.

the calorimeter, the individual hits could not be resolved, but were smeared out and appeared as noise. Heavier nuclei passed through the HRTs on average every 100 seconds or so. These generated heating spikes of up to several nK depending on the length of the track through the sensor assembly. An example of the HRT output obtained over a few hundred seconds is shown by the upper curve in Fig. 10. The lower curve shows ground data for comparison. Apart from the large spikes in the data, the effective noise was about 5 to 8 times the ground value. In addition, the spike events were almost always heating, leading to some bias in the averaged signals. At times of high particle flux, even higher noise than that shown was encountered. A detailed model of the effect of cosmic rays on the thermometer was developed and the results showed very similar behavior to that seen in the figure. This model also showed that the average heating caused a temperature offset between the thermometer and the helium sample of  $\sim 1$ -2 nK. The measurement of this offset is described below. Additional noise events were seen which correlated with large acceleration disturbances on the shuttle. We suspect that this effect was responsible for the occasional events that indicated apparent transient cooling of the HRTs. Special curve fitting techniques were used to minimize the effect of the spikes on the heat capacity results as described below.

### E. Heat Capacity Measurements

The initial flight heat capacity measurements were generated with the same software routines as used for the ground data. The first group of heat capacity measurements was a check on their apparent power dependence. The pulses were applied when the calorimeter was at

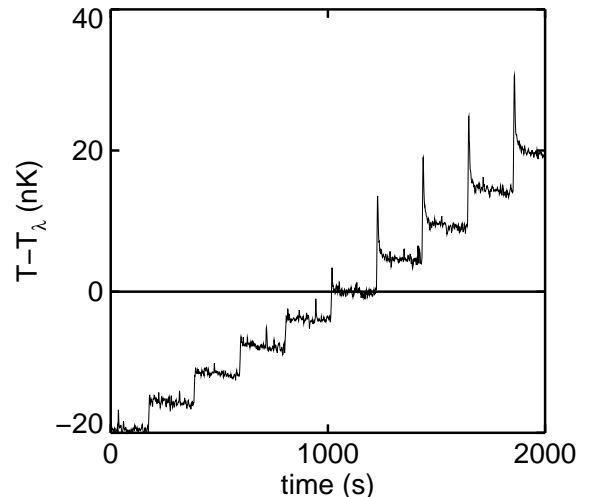


FIG. 11: High resolution temperature vs. time data containing a number of heat pulses with step heights of  $\sim 4$  nK. The estimated location of the lambda transition is marked.

2.1548 K and were similar to those used in pre-flight testing. The results were more noisy than on the ground, but otherwise showed no significant change. The apparent stray power was  $-9.77 \times 10^{-11}$  W. For comparison, the minimum power used in the flight measurements was  $1.7 \times 10^{-8}$  W. Also, the high power measurements showed a self-heating effect similar to that on the ground. Corrections were again applied for these effects. The second group of data consisted of wide range measurements performed in a similar manner to the ground. The other two groups of data were high resolution measurements spanning the region not accessible on the ground, and measurements above the transition. A set of high resolution measurements passing through the transition is shown in Fig. 11, with individual temperature steps of  $\sim 4$  nK. The growth of the relaxation time as the sample moves deeper into the normal phase is apparent. Measurements were made with step heights as small as 1 nK, but at this resolution the results were extremely noisy, with typical uncertainties of  $\sim 30\%$ . The practical limit to the resolution of the experiment from the point of view of heat capacity measurements was a step height of about 2 nK. Even here, a large amount of averaging was necessary to produce a usable result.

During the experiment 876 heat pulses were applied giving rise to 1752 temperature step measurements and heat capacity values. Approximately 3% of the measurements were abandoned due to excessive radiation heating, faulty telemetry records, or large external disturbances. Twenty-nine data points were deleted on the basis of being more than  $5\sigma$  from the best fit function. A number of data sets were timed to take advantage of the most favorable conditions: periods of low and stable radiation levels, quiet times on the shuttle and highest vacuum in the instrument. Some measurements were also

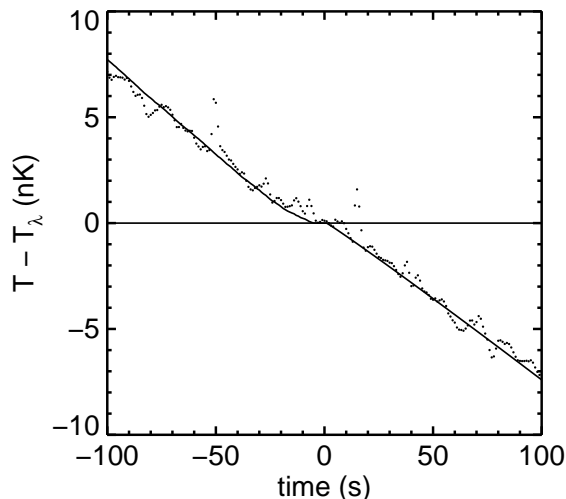


FIG. 12: An example of a cooling curve through the lambda point. Solid line is the result of a model calculation. The location of the lambda transition is determined by fitting the model to the data.

performed after the altitude of the shuttle was lowered from 288 to 210 km. This period was associated with a somewhat improved noise level in the HRTs but was unfortunately too brief to affect the overall accuracy of the experiment significantly. The conversion of the data to specific heat values is described in section VI.

### F. Lambda Point Location

As part of the process of generating the heat capacity data it was necessary to repeatedly cool the calorimeter back to a starting temperature for the next pulse sequence. A cooling ramp was initiated by reducing  $T_4$  sufficiently to cool the calorimeter at  $\sim 0.1$  nK/sec. As the sample cooled through the transition the outer layer of normal helium nearest the calorimeter wall converted to the superfluid state. The boundary between the two phases then propagated to the center of the sample in a time span of several seconds. While the helium was in this two-phase region,  $T_5$  paused very near  $T_\lambda$  until the temperature gradient within the helium was eliminated. When all of the helium was transformed into He-II, the sample cooled again, but at a slower rate than above the transition, due to the higher heat capacity in this region. This signature was very useful for keeping track of the apparent location of the lambda point on the flux scales of the HRTs. A typical cooling ramp is shown in Fig. 12. Also shown by the smooth curve is a model of the behavior fitted to the average cooling rate and adjusted to give the best estimate of  $T_\lambda$ . A few heating ramps were also performed, but these had a less clear transition signal due to the absence of the pause at the normal/superfluid phase boundary.

Some corrections need to be applied to the apparent lambda point flux readings to obtain the best estimates suitable for use with the heat capacity data. The major correction was due to the residual gas in the instrument vacuum space. This gas introduced a small temperature gradient in the calorimeter and HRT assembly related to the offset  $T_5 - T_4$  and to  $P_4$ . This was large enough that the variation of pressure with time introduced a detectable shift in the apparent lambda-transition temperature. It was therefore necessary to understand this effect well enough to correct the HRT temperature scales at times intermediate between lambda-point determinations. In addition to the general trend of pressure with time, there were two phenomena that helped us calibrate the effect. First, on the sixth day of the mission, a heater in the main helium bath was turned on briefly in an attempt to measure the amount of cryogen remaining. This event warmed the instrument walls, releasing some gas trapped there and causing a pressure increase lasting a number of hours. This resulted in a substantial change in the lambda-point flux readings over the same period. Second, we observed a rapid thermal transient in  $T_5$  when  $P_4$  was changed. This data allowed us to determine two pairs of parameters which appeared to be the most significant in a model of the gas effect. These parameters were the coefficients of the coupling between the HRT flux readings and  $T_4$ , and  $P_4$  at constant  $T_4$ . We found that the coupling to  $P_4$  was the more important of the two effects. For the lowest gas pressure in the mission, the coefficients for HRT #1 were 29.4 mK/W for the heater coefficient, and 0.11  $\mu\text{K}/\text{K}$  for the temperature coefficient. For HRT #2 we obtained 19.7 mK/W and 0.21  $\mu\text{K}/\text{K}$  respectively. At the start of the high resolution portion of the mission, the temperature coefficients were about a factor of two higher, due to the higher gas pressure. Fig. 13(a) shows the apparent location of the lambda point as a function of time for HRT #1. Fig. 13(b) shows the residuals after removing the modeled effects. The r.m.s. uncertainty of the corrected locations is  $\sim 0.3$  nK. Given the quality of the fit we estimate an uncertainty in the lambda temperature at any time after the start of the high resolution measurements of  $\pm 0.5$  nK.

### G. Charged Particle Data

It was observed that the heating rate of the calorimeter fluctuated slightly, typically with twice orbital period, preventing the calorimeter from reaching the level of thermal stability achieved on the ground. This variability was correlated with the readout of the CPMs. It can be seen in Fig. 14 which shows in the lower trace the temperature of the calorimeter over a 5000-second period where no pulses were applied. The upper trace shows the output from one of the CPM's over the same period averaged over 200 s intervals, clearly demonstrating the correlation. Correction factors were obtained by fitting

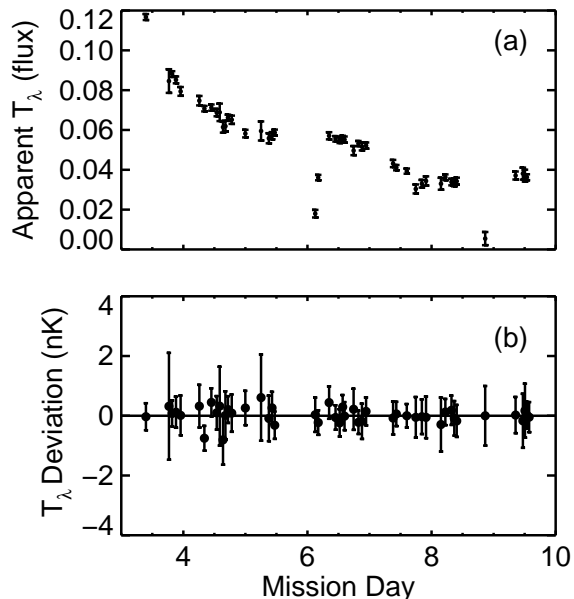


FIG. 13: a) Time dependence of the apparent HRT flux readings corresponding to the lambda transition during the high resolution phase of the mission. b) Residuals for the lambda point temperatures vs time after correction for pressure and charged particle heating effects.

the HRT variation vs. charged particle flux data with a 3-parameter function. The first parameter described the heat leak to stage 4 which is constant over the period of the data. The second parameter was proportional to the particle flux and was a measure of the heat input to the calorimeter due to cosmic rays. The third parameter accounted for the temperature offset between the HRT and the calorimeter due to cosmic ray energy dissipation in the HRT. We obtained temperature offsets for the two HRTs of 0.45 and 0.65 nK/count/sec, and a heat input to the calorimeter of  $1.29 \times 10^{-10}$  J/count, where the count number was derived from a model of the CPM responses to the known cosmic ray energy spectrum.<sup>57</sup> These correction factors were applied to all the high resolution thermometry data and the power input coefficient was used to correct the drift rate during heat capacity measurements. It was also found that for several hundred seconds after a passage through the radiation zone over the South Atlantic the heat capacity data appeared to be slightly affected. Data from this region were not used. A more detailed account of the charged particle observations is given elsewhere.<sup>57</sup>

## H. Accelerometer Data

A significant amount of accelerometer data was available during the mission. In addition to the peak acceleration in each 1-second interval, power spectral density

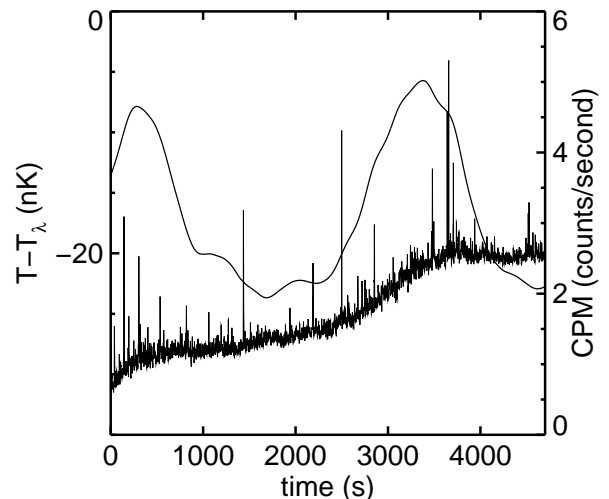


FIG. 14: Input data for calibrating the cosmic ray heating. Upper line: smoothed CPM data (right scale); lower line: raw HRT signal showing variation of calorimeter heating with time (left scale).

plots were available at approximately 100 min intervals and on special request. It was found that the peak acceleration amplitude was typically in the range  $0.5 - 1 \times 10^{-3}$  g with spikes to  $\sim 3 \times 10^{-3}$  g occurring approximately every few hundred seconds. From the larger acceleration events we were able to determine some characteristics of the acceleration sensitivity of the instrument. We found that the HRTs had a sensitivity to steady state acceleration, possibly due to changes of mechanical stress or some form of magnetic coupling. This was evident from HRT data collected during low power operation of the shuttle engines which applied a transverse acceleration to the instrument. The sensitivities of the two HRTs to this acceleration were 1.1 and 0.8  $\mu\text{K/g}$ . This indicates that some of the larger acceleration transients during normal operations should be visible on the HRTs. We searched for noise spike correlations with some of the largest events seen on the accelerometer output. A significant number of correlations were found, indicating that up to a few percent of the spikes in the HRT data were due to acceleration transients. However since there were clearly many more cases with no correlation, in the data analysis we elected to treat the acceleration spikes in the same manner as charged particle events. It was also apparent that most of the acceleration-related transients on the HRTs corresponded to heating.

The HRTs also showed a noise increase of about a factor of two during the low power operation of the shuttle engines. Since the acceleration noise increased by roughly a factor of eight during this period, it is unlikely that vibration contributed significantly to the noise level seen during normal operations. An apparent power input to the calorimeter averaging  $\sim 2 \times 10^{-9}$  W was also seen in this period. Linear extrapolation would indicate that

levels of  $2 - 3 \times 10^{-10}$  W might occur during normal heat capacity measurements, which is somewhat less than the measured charged particle dissipation level. However, this estimate is extremely crude, given the mechanical complexities involved. Our experience with low level vibration inputs on the ground indicated a highly nonlinear situation. The flight spectral information indicated highly variable vibration levels in the 1 Hz band centered on 55 Hz, and the corresponding heating estimate was approximately consistent with the above value. Further details of acceleration effects are available.<sup>30</sup>

## V. POST-FLIGHT MEASUREMENTS

After the instrument was returned to JPL it was operated in its flight configuration once more and a number of tests were performed to verify the stability of various parameters. Since the burst discs on the calorimeter were designed to rupture at the end of the flight, only tests with an empty calorimeter could be performed. Also since the cryostat had reached room temperature, the magnetic flux trapped in the HRTs was dissipated. The post-flight test activities were designed to improve the validation of the science data by showing that the calibration of various A/D converters and electronic circuits had not changed significantly from the pre-launch calibration.

Initially the electronics were operated alone using dummy loads to simulate the instrument. First, the calibrations of the bridges for the GRTs on the calorimeter were checked using a reference decade resistance box. It was found that the balance points of bridges #1 and 2 had changed by  $-0.7 \pm 0.1 \Omega$  and  $+0.8 \pm 0.1 \Omega$  over the range used. These shifts were small enough to be neglected. Next, the heater pulse shape was examined for changes in the transient behavior. No changes exceeding 10  $\mu$ s duration were detected. Also, the pulse timing was checked and found to be accurate to  $\pm 0.0003\%$ . The calibration of the A/D converter in the heater current monitoring circuit was checked. The results agreed with the pre-flight measurements to within 0.02% in power. Similar results verified correct operation for all the heater power ranges.

The electronics were reconnected to the instrument and the cryostat was cooled to  $\sim 2$  K. The calibrations of the A/D converters monitoring the calorimeter HRTs in terms of bits/ $\Phi_0$  were checked and found to be unchanged from flight to within 0.004%. This indicates that the converters and the SQUID feedback electronics were probably working normally during the flight. The temperature and power dependence of the resistance of the heater on the calorimeter were also remeasured. A zero-power resistance offset of 0.022% was found. The power dependence of the heater resistance was found to be about an order of magnitude higher than observed in the flight. It is conjectured that some damage occurred to the heater bonding when the calorimeter warmed up

after the mission. In the analysis below, the pre-flight value of the heater resistance was used.

A 100 Gauss field was then trapped in the HRT flux tubes and their sensitivities at the lambda point were verified to within 2%. During the following few years, the electronics system was used on a second flight experiment<sup>11</sup> and no significant anomalies were detected.

## VI. DATA ANALYSIS

In the ideal case the analysis of heat capacity data collected by the pulse method is straightforward. However, when high resolution measurements are attempted under adverse conditions a number of error sources need to be considered. The analysis of the raw data from the ground measurements was described earlier. Additional errors arise from operation in the space environment. In this section we describe the details of the flight specific heat calculations and our models of the associated corrections. We also describe the results of the curve fitting analysis.

### A. Specific Heat Calculation

The  $T_5$  drift data before and after each pulse were corrected for the heating of the calorimeter by cosmic rays. This correction term was determined from the CPM outputs as described earlier. These corrections were applied so that the temperature at the center of the heat pulse was undisturbed, allowing an accurate correspondence between the calculated midpoint temperature of a pulse and the original HRT temperature scale. The line fitting routine used to determine the intercepts was chosen to reduce the sensitivity of the results to the non-Gaussian spikes in the data.<sup>58</sup> The routine was also utilized to identify and remove the larger cosmic ray events from the data set. Spike events extending more than  $2.5\sigma$  from the fitted line were identified and removed, and a second fit performed. Model testing showed that these precautions reduced the bias in the heat capacity results substantially.

The statistical weight of the input temperature data, which is normally inversely proportional to the thermometer noise squared, was modified slightly to allow for the uncertainties in the heating rate corrections and the offset of the HRT temperature from the calorimeter temperature. The corrections had the effect of slightly deweighting the data at higher count rates as well as deweighting the data further from the center of the heat pulse where the correction becomes larger. The uncertainty in the heat capacity was derived from the usual partial derivatives and the uncertainties reported from the least squares fit. From a model of the effect of noise on the results we found that the heat capacity determined from the average of many noisy pulses,  $\langle C_p \rangle$ , was slightly greater than that determined from a noise-free pulse. It

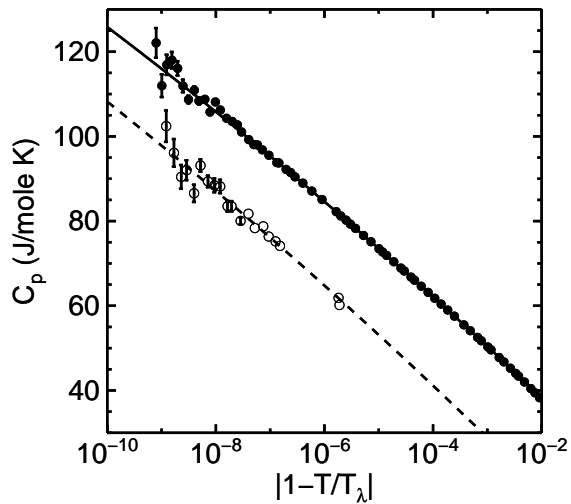


FIG. 15: Semi-logarithmic plot of the specific heat vs. reduced temperature over the full range measured. Below the transition the data (closed symbols) were binned with a density of 10 bins per decade, and above (open symbols) with a density of 8 bins per decade. Lines show best fits to the data.

is easy to show that  $\langle C_p \rangle / C_p = 1 + (\sigma_T / \Delta T)^2 + \dots$ . This correction term becomes important for very small step heights where averaging is used to improve the signal/noise ratio. All data were corrected for this effect using the statistical  $\sigma_T$  for the individual measurements. The curvature correction described earlier was also applied to the results, along with the path corrections given by Eqs. 6 and 7.

We found that we could decrease the scatter of the results by performing a more complex fit over all the pulses in a single data set simultaneously. This was accomplished by calculating the heat leak to stage 4 over many ( $N \sim 10$ ) pulses and performing a least squares fit with  $N$  temperature steps, one at each heat pulse. This reduces the total number of parameters determined for the  $N$  pulses: there is now only one straight line fit and  $N$  step heights compared to  $N$  line fits and  $N$  steps if each pulse is treated separately. This essentially takes advantage of the very long relaxation time for  $T_5$  to  $T_4$ , and assumes that the main perturbations to  $T_5$  have been modeled correctly. The specific heat results are shown in Fig. 15 after being bin-averaged at a density of 10 bins per decade of  $t$  below the transition, and 8 bins per decade above the transition. It can easily be seen that the specific heat divergence continues to the highest resolution we were able to achieve.

## B. High Temperature Data

Analysis of the data above  $T_\lambda$  was complicated by the finite thermal conductivity of the normal helium. This introduces a transient immediately after a heat pulse

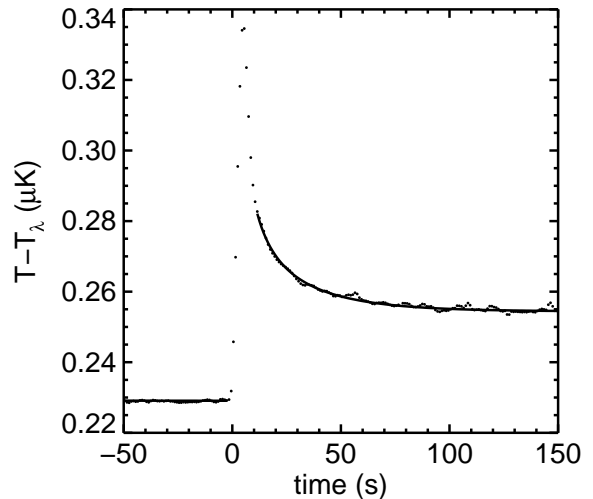


FIG. 16: Example of a HRT response to a heat pulse well above the lambda point. The lines are the results of a least squares fit to the data on each side of the pulse.

consisting of an overshoot in the temperature of the calorimeter shell and a rapid decay as the heat in the shell diffuses into the helium. An example of a pulse above the transition is shown in Fig. 16. The extra parameters required to allow for this effect increase the scatter of the heat capacity results. Furthermore, as the main objective of the experiment was to measure  $C_p$  below  $T_\lambda$ , only a few measurements were made above  $T_\lambda$ . The net result was a superior signal-to-noise ratio in the results below  $T_\lambda$ .

The thermal behavior of the shell was modeled using a radial diffusive heat flow approximation to the power input from the heater. This model was justified based on the very high conductivity of the calorimeter shell relative to the helium above the transition, the absence of convection in space and the high degree of isolation from the surroundings. An analytic solution to the problem of a transient heat input to the surface of an isolated solid sphere with diffusive heat flow is available.<sup>59</sup> The temperature of the surface as a function of time after the pulse is given by:

$$T_5 = T_f + \sum_{n=1}^{\infty} C_n \exp(-t/\tau_n) \quad (8)$$

where  $C_n$  are known coefficients determined by the initial conditions,  $\tau_n = C_p / (v\kappa\beta_n^2)$ ,  $v$  is the molar volume of the liquid,  $\kappa$  is its thermal conductivity,  $\beta_n$  are the positive roots of:  $\beta a \operatorname{ctn}(\beta a) = 1$ ,  $a$  is the radius of the sample and  $T_f$  is the final temperature. We used the first nine terms of this series to model the observed relaxation behavior. The ratios of the coefficients were obtained by modeling the transient heating of the calorimeter during the pulse and using the resulting temperature distribution as the initial condition for the solution to the ther-

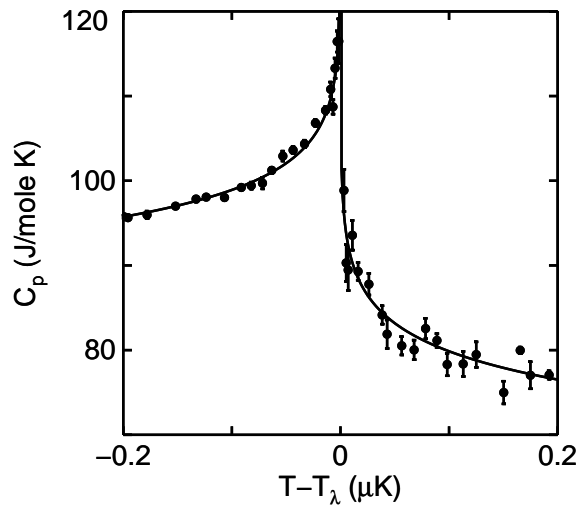


FIG. 17: Bin-averaged data close to the transition. Line shows the best fit function.

mal relaxation behavior of an isolated sphere. To allow for the variation of the properties of helium during the decay, the diffusivity,  $\nu\kappa/C_p$ , was modeled as having a locally linear dependence on the temperature within the sample. An example of a fit is shown by the solid line in Fig. 16. It can be seen that a reasonable representation of the behavior is obtained over a significant portion of the decay. The data above the transition became progressively more difficult to analyze as the temperature was increased. This was due primarily to the increased length of the extrapolation back to the center of the pulse after the thermal transient had decayed sufficiently. The bin averaged specific heat results near the transition are shown on a linear scale in Fig. 17.

### C. Curve Fitting

As described in the introduction, the RG theory makes a prediction for the critical exponent  $\alpha$ , describing the divergence of the heat capacity near the transition and for the ratio of the leading order coefficients on the two sides of the transition. The asymptotic form for the heat capacity near the transition is expected to be given by Eq.(1). We fit the results over the whole range measured with the truncated trial function:

$$\begin{aligned} C_p &= \frac{A^-}{\alpha} t^{-\alpha} (1 + a_c^- t^\Delta + b_c^- t^{2\Delta}) + B^- , \quad T < T_\lambda \\ &= \frac{A^+}{\alpha} |t|^{-\alpha} + B^- , \quad T > T_\lambda \end{aligned} \quad (9)$$

where we have assumed the constraint  $B^+ = B^-$ . The simpler form was used above  $T_\lambda$  because the data extend only to  $|t| \sim 10^{-6}$ , where the additional terms would still be negligible. All parameters were allowed to vary except for  $\Delta$ , which was fixed at its theoretical value<sup>25</sup> of 0.529,

and  $T_\lambda$ , which was determined as described earlier. See EPAPS<sup>60</sup> for the complete set of raw data used in the curve fitting. Also listed is the bin-averaged data set shown in Fig 15.

The best fit values for the parameters are listed in the first line of Table II along with the ratio  $A^+/A^-$ . The corresponding uncertainties are listed below the values and refer to the standard statistical error evaluated from the curve fitting routine. The uncertainties for the derived quantities  $A^+/A^-$  and  $P$  were evaluated by the usual formulae for propagation of errors<sup>61</sup> taking into account the strong correlation between the fitted parameters  $\alpha$ ,  $A^+$  and  $A^-$ . To obtain some feel for the sensitivity of the results to small changes in the analysis, we performed a number of extra fits to the data. The second group in the table shows the effect of modifying Eq.(9) to the form:

$$\begin{aligned} C_p &= \frac{A^-}{\alpha} t^{-\alpha} (1 + a_c^- t^\Delta) + b_c^- t + B^- , \quad T < T_\lambda \\ &= \frac{A^+}{\alpha} |t|^{-\alpha} + B^- , \quad T > T_\lambda \end{aligned} \quad (10)$$

which treats the third order term as a regular background contribution. It can be seen that the shift of  $\alpha$  is slightly outside the combined uncertainties, significantly larger than expected. This effect can be traced to the large value obtained for  $b_c^-$  which is much greater than the value of  $c_1$  (Eq. 3) estimated from the regular background contribution. It therefore appears that the second order Wegner term  $b_c^- t^{2\Delta}$  is the more important term to include in the fitting function, leading to Eq.(9) as the preferred representation of the behavior. This effect may be indicative of a rapid crossover to mean field behavior far from the transition. In the third and fourth groups we investigate the effect of reducing the fitting range at each end. Little effect is seen. The fifth group shows the sensitivity to a shift of the transition temperature of 1 nK, about twice the estimated uncertainty in the individual measurements. The next two groups show the effect of eliminating either the lowest or the highest power pulses from the fit. There is little dependence on the low power pulses as might be expected from their high uncertainties, but the high power pulses are important in the fit. For this case we also find the uncertainty in  $\alpha$  has increased by 75%. To lessen the dependence of the fit on the measurements with the greatest statistical weight, we set a lower limit of  $\sigma_C/C = 0.02\%$  and obtained the results in the eighth group. This constraint had little effect other than to increase the uncertainties of the parameters.

Taking into account the effects of the various constraints it appears that the flight results indicate  $\alpha = -0.0127 \pm 0.0003$  and  $A^+/A^- = 1.053 \pm 0.002$  with a high degree of confidence. These values can be compared with the theoretical estimates given in Table I. It can be seen that our result for  $\alpha$  falls between the two recent estimates, giving us confidence in the overall correctness of the RG approach. If the discrepancy between the two estimates can be resolved, a very high quality test of the

TABLE II: Results from curve fitting to the specific heat measurements using Eq.(9) except where noted. Statistical uncertainties are given in parentheses beneath the values.

Constraint	$\alpha$	$A^+/A^-$	$A^-$	$B^-$	$a_c^-$	$b_c^-$	$P$	Range of fit
Eq. (9)	-0.01264 (0.00024)	1.05251 (0.0011)	5.6537 (0.015)	460.19 (7.3)	-0.0157 (0.0015)	0.3311 (0.011)	4.154 (0.022)	$5 \times 10^{-10} < t < 10^{-2}$
Eq. (10)	-0.01321 (0.00025)	1.05490 (0.0011)	5.6950 (0.092)	443.76 (7.0)	-0.0253 (0.0015)	-128.4 (2.5)	4.155 (0.022)	$5 \times 10^{-10} < t < 10^{-2}$
Reduced range	-0.01254 (0.00043)	1.05210 (0.0018)	5.6458 (0.030)	463.11 (13.4)	-0.0136 (0.0043)	0.3035 (0.044)	4.154 (0.022)	$5 \times 10^{-10} < t < 3 \times 10^{-3}$
Reduced range	-0.01264 (0.00024)	1.05251 (0.0011)	5.6537 (0.015)	460.20 (7.4)	-0.0157 (0.0015)	0.3311 (0.012)	4.154 (0.022)	$10^{-9} < t < 10^{-2}$
$T_\lambda + 1$ nK	-0.01278 (0.00024)	1.05307 (0.0011)	5.6623 (0.015)	455.80 (7.2)	-0.0165 (0.0015)	0.3372 (0.012)	4.151 (0.022)	$5 \times 10^{-10} < t < 10^{-2}$
$P_5 > 10^{-7}$ W	-0.01269 (0.00026)	1.05273 (0.0012)	5.6570 (0.017)	458.55 (8.0)	-0.0160 (0.0017)	0.3335 (0.013)	4.154 (0.025)	$5 \times 10^{-10} < t < 10^{-2}$
$P_5 < 5 \times 10^{-4}$ W	-0.01323 (0.00042)	1.05498 (0.0018)	5.6970 (0.029)	443.27 (11.6)	-0.0228 (0.0038)	0.3853 (0.028)	4.156 (0.022)	$5 \times 10^{-10} < t < 10^{-2}$
$\sigma > 0.02\%$	-0.01275 (0.00041)	1.05297 (0.0018)	5.6620 (0.028)	456.89 (12.3)	-0.0176 (0.0034)	0.3473 (0.025)	4.154 (0.022)	$5 \times 10^{-10} < t < 10^{-2}$

theory would result. It is interesting to note that our result falls very close to the value  $-0.01294 \pm 0.0006$  obtained earlier by Kleinert.<sup>62</sup> This suggests that the earlier method of resumming the perturbation expansion may be more reliable than the more recent one.<sup>7</sup>

The value we obtain for the ratio  $A^+/A^-$  can be compared with the calculation of Strösser, Mönnigmann and Dohm<sup>9</sup> who's result for  $P$  implies  $A^+/A^- = 1.056 \pm 0.003$  if  $\alpha = -0.0127$ . For the value of  $P$  itself, we obtain  $P = 4.154 \pm 0.022$  where the uncertainty is the  $1\sigma$  statistical value including the effects of correlations of the parameters. This compares well with the Strösser et al. result of  $4.39 \pm 0.26$ . Very recently, Strösser and Dohm<sup>63</sup> have obtained the improved result  $P = 4.433 \pm 0.077$  from a 4-loop analytic calculation. On the experimental side, G. Ahlers has informed us<sup>64</sup> that his data<sup>55</sup> are consistent with  $P = 4.194 \pm 0.019$ , quite close to the present measurement. We note that the value of  $P$  is dependent on the heat capacity behavior above  $T_\lambda$  which is not very well established in our experiment. A value of  $P$  can also be derived from the data of Lipa and Chui.<sup>5</sup> From their published analysis, which did not constrain  $B^+ = B^-$ , we obtain  $P = 4.57 \pm 0.4$ . We note that the value of  $P$  and its uncertainty are significantly affected by the fitting constraint  $B^+ = B^-$ . This appears to be a result of the strong correlations between  $A^+$  and  $B^+$  and  $A^-$  and  $B^-$  in the curve fitting. If this constraint is added to the analysis of ref. 5 we obtain  $P = 3.98 \pm 0.02$ . More work would be valuable to determine an accurate value of  $P$ .

The quality of the fit to the model can be seen in Fig. 18 where the residuals from Eq.(9) are shown below the transition. Part (a) shows the bin-averaged results over the full range measured, and part (b) shows the individual measurements in the range  $t > 10^{-7}$ . The bin density

was 10 per decade, evenly spaced on a logarithmic scale. The parameters of the reference function are given in line 1 of Table II. Little curvature in the deviations at large  $t$  is evident, indicating residual effects from the truncation of the fitting function and from the calibration approximations are small. The deviation plot also shows that there is no indication of rounding from gravity or finite size effects near the transition. An estimate of the effect of the surface specific heat is shown by the broken curve. This result extends the agreement with the predicted behavior two orders of magnitude closer to the transition than previously.

The results given here for  $\alpha$  and  $A^+/A^-$  differ somewhat from those quoted in our preliminary analysis<sup>10</sup> after correction for a computational error.<sup>11</sup> Apart from the addition of the high power pulse data the main differences between the two analyses are improved modeling of the HRT calibrations and the power dependence of the heat capacity. Additional analysis has shown that approximately 90% of the change in  $\alpha$  is due to the improved calibration function in Eq.(5). Given the small change of  $\alpha$  that has resulted from this additional work, we have confidence that systematic effects are now well controlled and the present results are quite robust relative to alternative treatments of the raw measurements.

We can use our result for  $\alpha$  to perform a test of the Josephson scaling relation  $3\zeta + \alpha - 2 = 0$ . Using the result of Goldner et al<sup>18</sup> for  $\zeta$  we obtain  $3\zeta + \alpha - 2 = -0.0012 \pm 0.0019$  where the errors have been combined in quadrature. The agreement with the prediction is very good. Somewhat worse agreement is obtained if we use the result of Adriaans<sup>19</sup> which leads to  $3\zeta + \alpha - 2 = -0.0022 \pm 0.0005$ . We note that in both these experiments, the plots of deviations of the measurements from



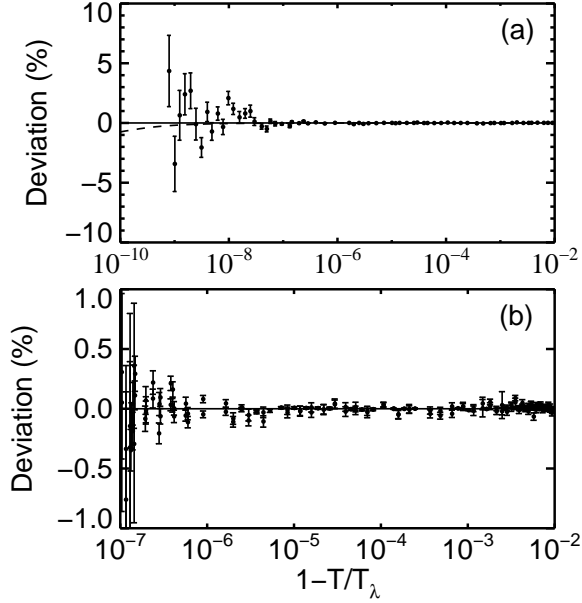


FIG. 18: a: Deviations of the bin averaged flight data from the best fit function vs reduced temperature on a semi-logarithmic scale below the transition. Dashed line: estimated surface specific heat term. b: Magnified view of deviations of individual measurements for  $t > 10^{-7}$ .

the fits show systematic departures, indicating that the error bars quoted may be optimistic. We also note that our results are in good agreement with the expected behavior based on vortex-ring RG theory.<sup>65</sup>

#### D. Thermal Conductivity

A secondary goal of the experiment was to obtain thermal conductivity results in the normal phase of helium above  $T_\lambda$ . As described in section VI-B, a series of time constants is derived from the fit to the thermal relaxation transient after a heat pulse. The thermal conductivity is inversely proportional to  $\tau_1$  and can therefore be output as part of the heat pulse analysis. As expected, we observe that the time constant of the decay is shortest near  $T_\lambda$  ( $\sim$  few seconds) and grows as the temperature rises. Very near  $T_\lambda$  where the pulse size is small, the transient is difficult to analyze: the small amplitude and short time constant are masked by the HRT noise, especially by the larger cosmic ray spikes which look very similar. This limited our analysis of  $\tau_1$  to  $|t| > 10^{-9}$ . The results for the thermal conductivity are shown in Fig. 19 after being binned at a density of 5 bins per decade of  $t$ . For comparison we show some results obtained in a ground experiment that covers part of the region.<sup>66</sup> Also shown is the behavior predicted by Dohm<sup>67</sup> using RG techniques. It can be seen that there is good agreement between the two sets of data and the theoretical model.<sup>68</sup>

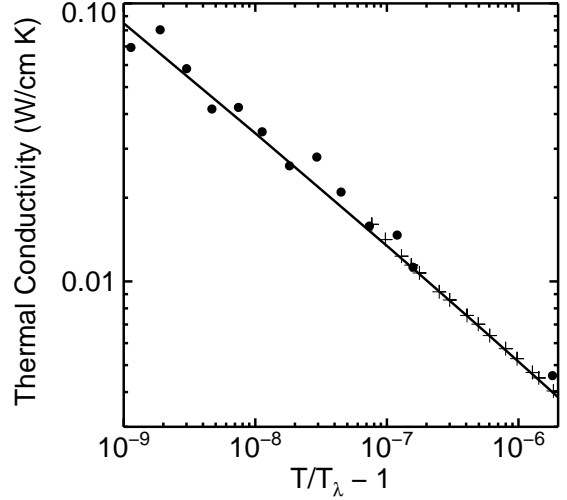


FIG. 19: Log-log plot of thermal conductivity vs reduced temperature above the lambda point. Filled circles: present work; +: Lipa and Li,<sup>66</sup> curve: model of Dohm.<sup>67</sup>

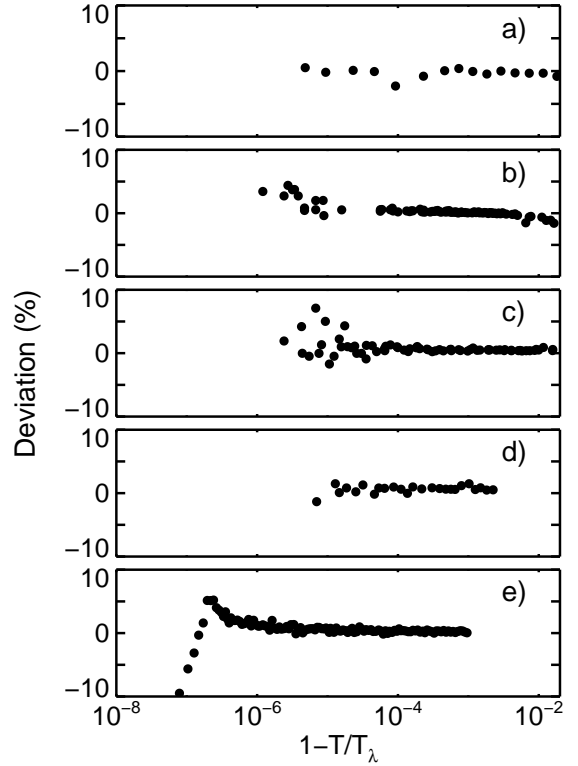


FIG. 20: Deviations of various data sets from the best fit function vs reduced temperature on a logarithmic scale, below the transition. a: Buckingham, Fairbank and Kellers;<sup>26</sup> b: Ahlers;<sup>55</sup> c: Gasparini and Moldover;<sup>16</sup> d: Takada and Watanabe<sup>69</sup> and e: Lipa and Chui.<sup>5</sup>

### E. Comparison with Other Measurements

In Fig. 20 we show the deviations of other sets of data from our best fit to Eq.(9). The data of Lipa and Chui<sup>5</sup> were obtained with a 3 mm high cell and that of Ahlers<sup>55</sup> with a 1.59 cm high cell. Although it is possible to correct for the effects of gravity, it can be seen that in the ground experiments the corrections become quite large near the transition, limiting access to the transition region. In Fig. 20(a,c,d) we show the deviations of other reported results<sup>16,26,69</sup> from the same function. It can be seen that there is reasonably good agreement between the various data sets, but occasionally the deviations are outside the noise of the data. Some of the discrepancies may be due to the use of earlier temperature scales, but it is unlikely that this effect contributes more than 0.2% to the deviations.

The significant improvement in scatter of the new data for  $t > 10^{-7}$  can be attributed to the use of the HRTs and a larger sample ( $\sim 0.8$  moles). The larger sample size does not directly improve the signal to noise of a heat capacity measurement, instead it attenuates the variations in the external heat leaks, leading to more accurate extrapolations to the center of a pulse.

### VII. CONCLUSION

In summary, our primary result is a new value of the exponent  $\alpha$  describing the divergence of the specific heat below the lambda-transition of helium with a reduced systematic uncertainty. This value is in good agreement with estimates based on RG calculations and is also in reasonable agreement with the value expected from su-

perfluid density data via the Josephson scaling relation. Our result for the ratio  $A^+/A^-$  is also in good agreement with recent estimates. Thermal conductivity measurements derived from the relaxation data are in reasonable agreement with steady state measurements further from the transition and with theoretical predictions.

This gives us additional confidence in the current model of second order transitions, and in the use of the results for other analyses. Other aspects of the RG theory, predicting the properties of condensed matter in general, need to be examined on their merits, but it is clear that the underlying principles are capable of explaining a wide range of properties of ordinary matter. We note that the reduction of the thermometer noise caused by cosmic rays that was demonstrated on a more recent mission<sup>11</sup> coupled with continuing advances in thermometry<sup>70</sup> opens up the possibility of further substantial reductions in the uncertainty of  $\alpha$  in future experiments.

### VIII. ACKNOWLEDGEMENTS

We wish to thank the NASA Office of Biological and Physical Research for its generous support with contract #JPL - 957448, and Dr. M. Lee for his long term support of the program. We greatly appreciate the support of the LPE teams at Stanford and JPL, and the services of the KSC and MSFC mission support teams. We also thank Ball Aerospace for extensive support with the development of the flight hardware, and especially G. Mills for the fabrication of the calorimeter. Lastly, we thank the crew of the Space Shuttle Columbia on STS-52 for their support during the microgravity periods of the mission.

---

\* jlipa@stanford.edu

<sup>1</sup> K. G. Wilson, Phys. Rev. B **4**, 3174 (1971). For a recent textbook on the subject, see H. Kleinert and V. Schulte-Frohlinde, *Critical Properties of  $\phi^4$  Theories* (World Scientific, Singapore, 2001).

<sup>2</sup> M. R. Moldover, J. V. Sengers, R. W. Gammon and R. J. Hocken, Rev. Mod. Phys., **51**, 79 (1979).

<sup>3</sup> A. Haupt and J. Straub, Phys. Rev. E, **59**, 1795 (1999).

<sup>4</sup> T. J. Edwards, thesis, University of Western Australia, 1984 (unpublished). See also Table I of ref. 3.

<sup>5</sup> J. A. Lipa and T. C. P. Chui, Phys. Rev. Lett., **51**, 2291 (1983).

<sup>6</sup> J. A. Lipa, *75th Jubilee Conference on Helium-4*, ed: J. G. M. Armitage (World Scientific, Singapore, 1983), p. 208.

<sup>7</sup> H. Kleinert, Physics Letts. A, **277**, 205 (2000). See also ch. 19 in the textbook cited in ref. 1.

<sup>8</sup> M. Campostrini, M. Hasenbusch, A. Pelissetto, P. Rossi and E. Vicari, Phys. Rev. B, **63**, 214503 (2001).

<sup>9</sup> See ref. 47 in M. Strösser and V. Dohm, Phys. Rev. E, **67**, 056115 (2003). See also the three-loop results in M. Strösser, M. Mönnigmann and V. Dohm, Physica B, **284-288**, 41 (2000) and H. Kleinert and B. Van den Bossche,

Phys. Rev. E **63**, 056113 (2001).

<sup>10</sup> J. A. Lipa, D. R. Swanson, J. A. Nissen, T. C. P. Chui and U. E. Israelsson, Phys. Rev. Lett., **76**, 944 (1996).

<sup>11</sup> See also footnote 15 of J. A. Lipa, D. R. Swanson, J. A. Nissen, Z. K. Geng, P. R. Williamson, D. A. Stricker, T. C. P. Chui, U. E. Israelsson and M. Larson, Phys. Rev. Lett., **84**, 4894 (2000).

<sup>12</sup> F. Wegner, Phys. Rev. B, **5**, 4529 (1972).

<sup>13</sup> V. Privman, P. C. Hohenberg and A. Aharony, in *Phase Transitions and Critical Phenomena*, eds: C. Domb and J. L. Lebowitz (Acad. N.Y. 1991), **14**, p. 1.

<sup>14</sup> M. Barmatz, P.C. Hohenberg and A. Kornblit, Phys. Rev. B, **12**, 1947 (1975).

<sup>15</sup> K. H. Mueller, G. Ahlers and F. Pobell, Phys. Rev. B, **14**, 2096 (1976).

<sup>16</sup> F. M. Gasparini and M. R. Moldover, Phys. Rev. B, **12**, 93 (1975).

<sup>17</sup> F. M. Gasparini and A. A. Gaeta, Phys. Rev. B, **17**, 1466 (1978).

<sup>18</sup> L. S. Goldner, N. Mulders and G. Ahlers, J. Low Temp. Phys., **93**, 131 (1992).

<sup>19</sup> M. J. Adriaans, D. R. Swanson and J. A. Lipa, Physica B,

- 194-196, 733 (1994).
- <sup>20</sup> G. Ahlers in: *The Physics of Liquid and Solid Helium*, eds: K. H. Bennemann and J. B. Ketterson (Wiley, N.Y. 1976) Part 1, p. 85.
- <sup>21</sup> R. Schloms and V. Dohm, *Europhys. Letts.*, **3**, 413 (1987).
- <sup>22</sup> D. S. Greywall and G. Ahlers, *Phys. Rev. A*, **7**, 2145 (1973).
- <sup>23</sup> A. Singaas and G. Ahlers, *Phys. Rev. B*, **30**, 5103 (1984).
- <sup>24</sup> R. Schloms and V. Dohm, *Phys. Rev. B*, **42**, 6142 (1990).
- <sup>25</sup> R. Guida and J. Zinn-Justin, *J. Phys. A*, **31**, 8103 (1998).
- <sup>26</sup> W. M. Fairbank, M. J. Buckingham and C. F. Kellers, *Proc. 5th Int. Conf. on Low Temp. Phys.* (Madison, Wis. 1957), p. 50.
- <sup>27</sup> See for example, G. Ahlers, *Phys. Rev.*, **171**, 275 (1968); and M. Barmatz and I. Rudnick, *Phys. Rev.*, **170**, 224 (1968).
- <sup>28</sup> J. A. Lipa, D. R. Swanson, J. A. Nissen and T. C. P. Chui, *Cryogenics*, **34**, 341 (1994).
- <sup>29</sup> T.S. Luchik, U. E. Israelsson, D. Petrac and S. Elliott, *Adv. Cryo. Eng.*, **41**, 1135 (1996).
- <sup>30</sup> J. A. Nissen, D. R. Swanson, D. A. Stricker and J. A. Lipa, AIAA paper #2000 – 0943.
- <sup>31</sup> Nippon Mining Co. Japan, grade 6N (99.9999% pure).
- <sup>32</sup> J. G. Hurst and A. B. Lankford, U.S. Department of Commerce NBSIR 84-3007, (1984). See also S. S. Rosenblum, W. A. Steyert and F. R. Fickett, *Cryogenics*, **17**, 645 (1977).
- <sup>33</sup> J. A. Lipa, B. C. Leslie and T. C. Wallstrom, *Physica* **107 B**, 331 (1981); T. C. P. Chui, D. R. Swanson, M. J. Adriaans, J. A. Nissen, and J. A. Lipa, *Temperature, its Measurement and Control in Science and Industry*, **6**, 1213 (1992) and T. C. P. Chui, D. R. Swanson, M. J. Adriaans, J. A. Nissen, and J. A. Lipa, *Phys. Rev. Lett.*, **69**, 3005 (1992).
- <sup>34</sup> E. Velu, J. -P. Renard and B. Lecuyer, *Phys. Rev. B*, **14**, 5088 (1976).
- <sup>35</sup> D. R. Swanson, J. A. Nissen, T. C. P. Chui, P. R. Williamson and J. A. Lipa, *Physica B*, **194**, 25 (1994).
- <sup>36</sup> D. Marek, *Jap. J. App. Phys.*, **26**, 1683 (1987).
- <sup>37</sup> Williams Mfg. Corp., San Jose, Calif.
- <sup>38</sup> J. Luu, T. C. P. Chui and J. A. Lipa, *Proc. Internat. Conf. on Low Temp. Phys. (LT-17)*, eds: U.Eckern et al. (Karlsruhe, 1984), p. 207.
- <sup>39</sup> K. W. Rigby, D. Marek and T. C. P. Chui, *Rev. Sci. Instrum.*, **61**, 834 (1990).
- <sup>40</sup> Vacuumschmelze GMBH, Germany.
- <sup>41</sup> Biomagnetic Technologies Inc., San Diego, CA.
- <sup>42</sup> P. Mason, D. Collins, P. Cowgill, D. Elleman, D. Petrac, M. Saffren and T. Wang, *Adv. Cryo. Eng.*, **25**, 801 (1980).
- <sup>43</sup> D. Petrac, U. E. Israelsson, and T. S. Luchik, *Adv. Cryo. Eng.*, **39**, 137 (1994).
- <sup>44</sup> See, for example, M. J. B. Rogers, K. Hrovat and M. Moskowicz, *Adv. Space Res.*, **22**, No. 8, 1257 (1998).
- <sup>45</sup> Lakeshore Cryotronics, Westerville, OH, Model # RF-800-2, SN. B109B.
- <sup>46</sup> Lakeshore Cryotronics, 1.2 - 22 K range.
- <sup>47</sup> H. Preston-Thomas, *Metrologia*, **27**, 3 (1990), and *ibid.* p. 107.
- <sup>48</sup> L. G. Rubin and Y. Golahny, *Rev. Sci. Instrum.*, **43**, 1758 (1972).
- <sup>49</sup> Electro Scientific Industries, Portland, OR, Model # RS-925, SN. 623012.
- <sup>50</sup> Y. K. Leung and J. F. Kos, *Cryogenics*, **19**, 531 (1979).
- <sup>51</sup> H. B. Callen and T. A. Welton, *Phys. Rev.*, **83**, 34 (1951).
- <sup>52</sup> X. Qin, J. A. Nissen, D. R. Swanson, P. R. Williamson, D. A. Stricker, J. A. Lipa, T. C. P. Chui and U.E. Israelsson, *Cryogenics*, **36**, 781 (1996).
- <sup>53</sup> E. C. Kerr and R. D. Taylor, *Ann. Phys.*, **26**, 292 (1964); J. J. Niemela and R. J. Donnelly, *J. Low Temp. Phys.*, **98**, 1 (1995).
- <sup>54</sup> C. F. Kellers, thesis, Physics Dept., Duke University, Durham, NC, (1960).
- <sup>55</sup> G. Ahlers, *Phys. Rev. A*, **3**, 696 (1971). (We note some typographical errors in Eq's (7) and (10) of this paper.)
- <sup>56</sup> J. A. Nissen, D. R. Swanson, X. Qin and J. A. Lipa, *Czech. J. Phys.*, **46-S1**, 379 (1996).
- <sup>57</sup> P. R. Williamson, J. A. Nissen, D. R. Swanson and J. A. Lipa, *Proc. 24th Int. Cosmic Ray Conf.* (Rome, Italy, Aug. '95), **4**, p.1287.
- <sup>58</sup> W. H. Press, B. P. Flannery, S. A. Teukolsky and W. T. Vetterling, *Numerical Recipes* (Cambridge University Press, Cambridge, 1987), p. 539.
- <sup>59</sup> M. Necati Ozisik, *Boundary Value Problems of Heat Conduction*, (Dover, NY 1989).
- <sup>60</sup> The complete set of raw data used in the curve fitting is listed in EPAPS Document No. [number to be inserted by publisher]. Also listed is the bin-averaged data set shown in Fig 15. A direct link to this document may be found in the online article's HTML reference section. The document may also be reached via the EPAPS homepage (<http://www.aip.org/pubservs/epaps.html>) or from <ftp.aip.org> in the directory /epaps/. See the EPAPS homepage for more information.
- <sup>61</sup> P. R. Bevington, *Data Reduction and Error Analysis for the Physical Sciences*, (McGraw-Hill Book Co., NY, 1969), p. 66.
- <sup>62</sup> H. Kleinert, *Phys. Rev. D*, **60**, 085001 (1999).
- <sup>63</sup> M. Strösser and V. Dohm, *Phys. Rev. E* (to be published).
- <sup>64</sup> G. Ahlers, private communication.
- <sup>65</sup> G. A. Williams, *J. Low Temp. Phys.*, **101**, 421 (1995).
- <sup>66</sup> Derived from the results in: J. A. Lipa and Q. Li, *Czech. J. Phys.*, **46**, 185 (1996) Suppl. S1.
- <sup>67</sup> V. Dohm, *Phys. Rev. B*, **44**, 2697 (1991).
- <sup>68</sup> We note that the theoretical curve in Fig. 3 of ref. 10 was drawn slightly too low.
- <sup>69</sup> T. Takada and T. Watanabe, *J. Low Temp. Phys.*, **41**, 221 (1980).
- <sup>70</sup> B. J. Klemme, M. J. Adriaans, P. K. Day, D. A. Sergatskov, T. L. Aselage and R. V. Duncan, *J. Low Temp. Phys.*, **116**, 133 (1999).